

**REPUBLIC OF TURKEY  
YILDIZ TECHNICAL UNIVERSITY  
GRADUATE SCHOOL OF NATURAL AND APPLIED SCIENCES**

**INVESTIGATION OF ELASTOMERIC BEARINGS' BEHAVIOR  
UNDER FATIGUE LOADING**



**KADİR EKŞİ**

**MSc. THESIS  
DEPARTMENT OF CIVIL ENGINEERING  
PROGRAM OF STRUCTURAL ENGINEERING**

**ADVISER  
ASSIST. PROF. FATİH ALEMDAR**

**İSTANBUL, 2019**

**REPUBLIC OF TURKEY**  
**YILDIZ TECHNICAL UNIVERSITY**  
**GRADUATE SCHOOL OF NATURAL AND APPLIED SCIENCES**

**INVESTIGATION OF ELASTOMERIC BEARINGS' BEHAVIOR**  
**UNDER FATIGUE LOADING**

- A thesis submitted by Kadir EKŞİ in partial fulfillment of the requirements for the degree of **MASTER OF SCIENCE** is approved by the committee on 10.05.2019 in Department of Civil Engineering, Structural Engineering Program.

**Thesis Adviser**

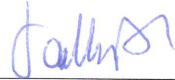
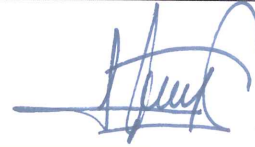

Assist. Prof. Dr. Fatih ALEMDAR  
Yıldız Technical University

**Approved by the Examining Committee**

Assist. Prof. Dr. Fatih ALEMDAR  
Yıldız Technical University

Assoc. Prof. Dr. Serkan BEKİROĞLU  
Yıldız Technical University

Assist. Prof. Dr. Sami And KILIÇ  
Boğaziçi University

  
\_\_\_\_\_  
  
\_\_\_\_\_  
  
\_\_\_\_\_

## ACKNOWLEDGEMENTS

---

I would first like to thank my thesis adviser Assist. Prof. Fatih Alemdar who was always encouraging, reachable and ready to guide me when I needed. His great efforts in his office and in laboratory ensured me to complete this study. I also thank to Development Agency for the support in project named “Elastomeric Bearing Test Center”, Project No: TR10 / 15 / YNK / 034.

I thank Metal Yapi A.Ş. management for their support to complete my courses and my thesis. I am especially thankful to my manager, İlknur Akın, who has always been polite and understanding.

Finally, I am extremely grateful to my family, for their endless supports during all the challenges I was in.

May, 2019

Kadir EKŞİ

## TABLE OF CONTENTS

---

	Page
LIST OF SYMBOLS .....	vi
LIST OF ABBREVIATIONS .....	vii
LIST OF FIGURES .....	viii
LIST OF TABLES .....	xii
ABSTRACT .....	xiii
ÖZET .....	xv
CHAPTER 1	
1.1 Literature Review .....	1
1.2 Objective of the Thesis .....	2
1.3 Hypothesis .....	2
CHAPTER 2	
GENERAL INFORMATION .....	3
2.1 The Concept of Base Isolation .....	3
2.2 Common Base Isolators .....	5
2.2.1 Sliding Isolation Systems .....	6
2.2.2 Elastomeric Isolation Systems .....	7
2.3 Energy Dissipation Devices .....	9
CHAPTER 3	
STEEL-LAMINATED ELASTOMERIC BEARINGS .....	12

3.1	Compression Stiffness .....	13
3.2	Hardness.....	17
3.3	Shear Modulus .....	18
CHAPTER 4		
EXPERIMENTAL STUDIES .....		22
4.1	Determination of the Shear Modulus.....	27
4.2	Shear Stiffness under Different Pressure Loading.....	31
CHAPTER 5		
COMPUTER-AIDED ANALYSIS .....		44
5.1	Finite Element Model .....	45
5.2	Mesh Elements and Overcoming the Convergence Failure.....	46
5.3	Hyperelastic Material Models.....	50
5.4	Hyperelastic Material Definition in ANSYS Workbench .....	54
5.5	Executing Finite Element Analyses .....	55
CHAPTER 6		
RESULTS AND DISCUSSION.....		64
REFERENCES .....		73
CURRICULUM VITAE.....		75

## LIST OF SYMBOLS

---

$C_{ij}$	Material constants
$d$	Material incompressibility
$E$	Young's Modulus
$E_s$	Compression Modulus
$G$	Shear Modulus
$I_1$	First deviatoric strain invariants
$I_2$	Second deviatoric strain invariants
$J$	Ratio of the deformed volume over undeformed volume
$K$	Bulk Modulus
$W$	Strain energy function
$\lambda_i$	Principal stretches
$\mu$	Initial shear modulus
$\nu$	Poisson's ratio

## LIST OF ABBREVIATIONS

---

AASHTO	American Association of State Highway and Transportation Officials
ASTM	American Society for Testing and Materials
IRHD	International Rubber Hardness Degree
ISO	International Organization for Standardization

## LIST OF FIGURES

---

	Page
Figure 2.1 Principles of conventional (a) and base isolated (b) structures [3] .....	4
Figure 2.2 Period shift of a structure with base isolation [4].....	5
Figure 2.3 Different stages during the displacement of a single pendulum bearing [3].	6
Figure 2.4 Different stages during the displacement of a triple pendulum bearing [3]..	6
Figure 2.5 Flat sliding bearing system [5] .....	7
Figure 2.6 Possible deformations of bearings; (a) compression (b) shear (c) rotation [6] .....	7
Figure 2.7 Steel-laminated elastomeric bearing (a) and lead-rubber bearing (b) [7].....	8
Figure 2.8 Shear force – Displacement behavior of a low-damping elastomeric bearing .....	8
Figure 2.9 Shear force – Displacement behavior of a high-damping elastomeric bearing.....	9
Figure 2.10 Shear force – Displacement behavior of a lead-rubber elastomeric bearing.	9
Figure 2.11 Different installation types of fluid viscous dampers.....	10
Figure 2.12 Pall frictional damper [11] .....	11
Figure 3.1 Steel-laminated elastomeric bearing [12].....	12
Figure 3.2 Bulging effect .....	13
Figure 3.3 Section views of elastomeric bearings with different inner layers.....	14
Figure 3.4 3D view of a bearing .....	15
Figure 3.5 Bearings with different inner layers under same compression load.....	16
Figure 3.6 Inclined compressive test set-up [22] .....	19
Figure 3.7 Inclined compressive test stress-strain graph [22] .....	19
Figure 3.8 Quad shear test set-up [13].....	20
Figure 3.9 Quad shear test stress-strain graph [13] .....	20
Figure 4.1 Instron 8803 Fatigue Testing System .....	22



Figure 4.2	Compression loading .....	23
Figure 4.3	Stress-Strain graph under compression loading .....	24
Figure 4.4	Stress-Strain graph under compression loading (low strain levels) .....	25
Figure 4.5	Stress-Strain graph under compression loading (high strain levels) .....	26
Figure 4.6	Steel parts used for the determination of shear modulus.....	27
Figure 4.7	Test set-up .....	28
Figure 4.8	Deformation along shear direction .....	29
Figure 4.9	Hysteresis loop obtained from five cycles .....	30
Figure 4.10	Hysteresis loop obtained from only the sixth cycle .....	30
Figure 4.11	Values for the determination of shear modulus.....	31
Figure 4.12	Steel parts used for the experiment .....	32
Figure 4.13	Preparation for the experiment .....	33
Figure 4.14	Test set-up for phase one.....	34
Figure 4.15	Bonding Failure during the first phase .....	35
Figure 4.16	Squeezing the nuts after the first phase .....	35
Figure 4.17	Test set-up for the phase two.....	36
Figure 4.18	Movement along shear direction .....	37
Figure 4.19	100 <sup>th</sup> cycle under 3 MPa compression.....	38
Figure 4.20	1000 <sup>th</sup> cycle under 3 MPa compression.....	38
Figure 4.21	5000 <sup>th</sup> cycle under 3 MPa compression.....	39
Figure 4.22	10000 <sup>th</sup> cycle under 3 MPa compression.....	39
Figure 4.23	100 <sup>th</sup> cycle under 4.5 MPa compression.....	40
Figure 4.24	1000 <sup>th</sup> cycle under 4.5 MPa compression.....	40
Figure 4.25	5000 <sup>th</sup> cycle under 4.5 MPa compression.....	41
Figure 4.26	10000 <sup>th</sup> cycle under 4.5 MPa compression.....	41
Figure 4.27	100 <sup>th</sup> cycle under 6 MPa compression.....	42
Figure 4.28	1000 <sup>th</sup> cycle under 6 MPa compression.....	42
Figure 4.29	5000 <sup>th</sup> cycle under 6 MPa compression.....	43
Figure 4.30	10000 <sup>th</sup> cycle under 6 MPa compression.....	43
Figure 5.1	3D model and dimensions (mm) of the bearing sample model.....	45
Figure 5.2	Illustration of the SOLID70 type of mesh element .....	46
Figure 5.3	Illustration of the SOLID187 type of mesh element .....	47

Figure 5.4	Illustration of the SOLID185 type of mesh element .....	47
Figure 5.5	Illustration of the SOLID186 type of mesh element .....	48
Figure 5.6	Displacement convergence graph.....	49
Figure 5.7	Error message emphasizing element distortions .....	49
Figure 5.8	Warning message emphasizing high computational cost.....	50
Figure 5.9	Ultimate mesh condition of the finite element model .....	50
Figure 5.10	Stress-Strain graphs with none (a), one (b) and two (c) inflection points...	52
Figure 5.11	Hyperelastic material models in ANSYS .....	54
Figure 5.12	Required material constants .....	54
Figure 5.13	Hyperelastic experimental data modules.....	55
Figure 5.14	Required test data for the determination of material constants .....	55
Figure 5.15	Modified stress-strain graphs .....	56
Figure 5.16	Deformed shape at 17% strain (7 mm).....	57
Figure 5.17	Deformed shape at 33% strain (14 mm).....	57
Figure 5.18	Deformed shape at 50% strain (21 mm).....	57
Figure 5.19	Axial deformation under 3 MPa compression load (14 <sup>th</sup> Step).....	58
Figure 5.20	Lateral deformation at 17% strain (21 <sup>st</sup> Step) (Under 3 MPa compression).....	58
Figure 5.21	Lateral deformation at 33% strain (28 <sup>st</sup> Step) (Under 3 MPa compression).....	59
Figure 5.22	Lateral deformation at 50% strain (35 <sup>th</sup> Step) (Under 3 MPa compression).....	59
Figure 5.23	Axial deformation under 4.5 MPa compression load (14 <sup>th</sup> Step).....	60
Figure 5.24	Deformed shape at 17% lateral strain (21 <sup>st</sup> Step) (Under 4.5 MPa compression).....	60
Figure 5.25	Deformed shape at 33% lateral strain (28 <sup>st</sup> Step) (Under 4.5 MPa compression).....	60
Figure 5.26	Deformed shape at 50% lateral strain (35 <sup>th</sup> Step) (Under 4.5 MPa compression).....	61
Figure 5.27	Axial deformation under 6 MPa compression load (14 <sup>th</sup> Step).....	61
Figure 5.28	Deformed shape at 17% lateral strain (21 <sup>st</sup> Step) (Under 6 MPa compression).....	62
Figure 5.29	Deformed shape at 33% lateral strain (28 <sup>st</sup> Step) (Under 6 MPa compression).....	62
Figure 5.30	Deformed shape at 50% lateral strain (35 <sup>th</sup> Step) (Under 6 MPa compression).....	62
Figure 6.1	Change at lateral behavior through cycles (3 MPa compression).....	64

Figure 6.2	Change at lateral behavior through cycles (3 MPa compression) .....	65
Figure 6.3	Change at lateral behavior through cycles (4.5 MPa compression) .....	65
Figure 6.4	Change at lateral behavior through cycles (6 MPa compression) .....	65
Figure 6.5	Graphical illustration of damping ratios through cycles under various compression loads .....	66
Figure 6.6	Change of maximum lateral reaction forces through cycles under 50% lateral strain (Experimental study) .....	67
Figure 6.7	Lateral reaction forces (kN) through cycles for each sample (Experimental study) .....	68



## LIST OF TABLES

---

	Page
Table 3.1 Relation between IRHD and shear modulus for elastomers [20] .....	18
Table 3.2 Relation between shore A durometer and shear modulus for elastomers [21]	18
Table 5.1 Reaction forces at specified lateral strain level (without compression load) .	57
Table 5.2 Reaction forces at specified lateral strain level (3 MPa compression load) ...	59
Table 5.3 Reaction forces at specified lateral strain level (4.5 MPa compression load)	61
Table 5.4 Reaction forces at specified lateral strain level (6 MPa compression load) ...	63
Table 6.1 Damping ratios of bearing samples under specified conditions (%) .....	66
Table 6.2 Lateral reaction forces (kN) for each sample (Experimental study).....	68
Table 6.3 Lateral reaction forces without compression load .....	69
Table 6.4 Axial displacements under specified compression load .....	69
Table 6.5 Comparisons of the results of experimental study and finite element model (3 MPa Compression).....	70
Table 6.6 Comparisons of the results of experimental study and finite element model (4.5 MPa Compression).....	70
Table 6.7 Comparisons of the results of experimental study and finite element model (6 MPa Compression).....	70

## ABSTRACT

---

# INVESTIGATION OF ELASTOMERIC BEARINGS' BEHAVIOR UNDER FATIGUE LOADING

Kadir EKŞİ

Department of Civil Engineering

MSc. Thesis

Adviser: Assist. Prof. Fatih ALEMDAR

According to the traditional approach, structures are designed to mainly resist vertical loads. This approach may lead to poor conditioning along horizontal ground movements occur during an earthquake. Although there are significant improvements in Earthquake Engineering to design the structures with a certain level of earthquake performance, base isolation is used mainly at strategically important structures to reduce the earthquake-induced damage. The modern concept of base isolation works by decoupling the upper-structure from sub-structure. The aim is to reduce the transmission of the earthquake loads to the upper-structure by taking advantage of the horizontal flexibility of the bearings.

Elastomeric bearings are one of the most commonly used seismic isolation systems in the market. These bearings are generally consist of vulcanized rubber blocks bonded to steel plates. Rubber blocks provide the flexibility, while the steel plates provide axial rigidity. Although the steel plates have nearly no effect to lateral behavior, they are essential to provide the sufficient axial stiffness in order to transmit vertical loads to foundation properly.

Elastomeric bearings make the horizontal movements under continuous compression loads. This situation is the starting point of the thesis. In this study, behaviors of elastomeric bearing samples with a 100 mm x 100 mm plan dimensions cut from a full-size bearing were examined under different conditions. As a start, compression stiffness and shear modulus of the bearings were determined by using the methods close to ones clarified in AASHTO and ASTM Specifications. Later, the change at lateral behavior was observed during repetitive dynamic lateral movement under 3, 4.5 and 6 MPa

compression load levels and the results were compared. It was observed that the lateral stiffness decreases as the compression load increases.

After the experimental studies were executed, the finite element model of a bearing sample was prepared by using 5-Parameter Mooney-Rivlin Hyperelastic Material Model. Since some essential test data for simulating the behavior of the rubber material accurately are missed, stress-strain graphs of another rubber material which were found in software documentation were modified with shear data obtained from the experimental studies. Analyses were executed by using the material constants obtained from the modified graphs. Although being lack of some test data for rubber material, accurate results were achieved -especially for lateral behavior- on certain strain levels.

**Key words:** Elastomeric bearings, seismic isolators, earthquake engineering, civil engineering, fatigue loading



# ELASTOMERİK MESNETLERİN YORULMA YÜKLEMESİ ALTINDAKİ DAVRANIŞLARININ İNCELENMESİ

Kadir EKŞİ

İnşaat Mühendisliği Anabilim Dalı  
Yüksek Lisans Tezi

Tez Danışmanı: Dr. Öğretim Üyesi Fatih ALEMDAR

Geleneksel yaklaşıma göre, yapılar genellikle esas olarak düşey yüklere direnecek şekilde dizayn edilmişlerdir. Bu durum deprem sırasında oluşan yatay hareketlere karşı zayıf bir davranışa yol açabilir. Günümüzde yapıların belli seviyede deprem performansı sergileyebilmesi için Deprem Mühendisliği alanında önemli gelişmelerin olmasının yanında, özellikle stratejik öneme sahip yapılarda deprem kaynaklı hasarların azaltılması için temel izolasyon sistemleri kullanılır. Temel izolasyonunun mantığı üst yapıyla alt yapıyı birbirinden ayırmaktır. Amaç izolatörlerin yatay esnekliklerinden faydalanarak üst yapıya aktarılan deprem yüklerinin azaltılmasıdır.

Elastomerik mesnetler piyasadaki en çok kullanılan sismik izolasyon sistemlerinden biridir. Bu mesnetler çelik plakalarla birleşmiş volkanize kauçuk bloklardan oluşur. Kauçuk bloklar mesnetin esnekliğini sağlarken çelik plakalar ise düşey rijitliğini sağlarlar. Çelik plakaların mesnedin yatay davranışına hemen hemen hiç etkisi olmamasına karşın, düşey yüklerin düzgün bir biçimde temele aktarılabilmesi açısından çok önemlidirler.

Elastomerik mesnetler yatay hareketlerini sürekli bir basınç kuvveti altında yaparlar. Bu durum tezin başlangıç noktasıdır. Bu çalışmada, tam boy elastomerik mesnetten 100 mm x 100 mm plan boyutlarında kesilmiş numunelerin davranışları farklı koşullar altında incelenmiştir. Başlangıç olarak numunelerin basınç rijitliği ve kayma modülü AASHTO ve ASTM standartlarında belirtilen yöntemlere yakın bir şekilde belirlenmiştir. Sonrasında 3, 4.5 ve 6 MPa basınç yükleri altında tekrarlı yatay yükleme sırasındaki davranışları gözlenmiş ve sonuçlar karşılaştırılmıştır. Basınç değeri arttıkça yatay rijitliğin azaldığı gözlenmiştir.

Deneysel alıřmaların tamamlanmasından sonra, 5 Parametrelil Mooney-Rivlin hiperelastik malzeme modeli kullanılarak mesnet numunesinin sonlu eleman modelleri yapılmıřtır. Kauuk malzeme davranıřını tam olarak simule edebilmek iin gerekli olan bazı test dataları eksik olduėu iin program datasında bulunan bir kauuk malzemenin gerilme-gerinme grafiėi, bu alıřmada elde edilen kayma davranıřıyla modifiye edilerek kullanılmıřtır. Modifiye edilmiř olan grafiėe uygun malzeme katsayıları elde edilerek analizler gerekleřtirilmiřtir. Sonu olarak, belirtilen bazı data eksikliklerine raėmen belirli gerinme seviyelerinde -zellikle yanal davranıřta- deneysel sonulara olduka yakın deėerler elde edilmiřtir.

**Anahtar Kelimeler:** Elastomerik mesnetler, sismik izolatrler, deprem mhendisliėi, inřaat mhendisliėi, yorulma yklemesi





#### 1.1 Literature Review

Turkey is located on one of the most active earthquake zones called Mediterranean-Alpine-Himalayan. Between 1900 and 2005, the number of earthquakes that occurred between the magnitudes 5-5.9 is 1170, 6-6.9 is 155 and 7-8 is 34 [1]. These earthquakes have caused significant life loss and great damage to man-made structures. In Turkey, seismic isolation concept had started to gain importance especially after the Marmara Earthquake dated 1999. Until 2018, there were no code or standard to design a building with seismic isolation systems in Turkey. Currently, new Turkish Earthquake Code (2018) includes the design criteria for the buildings under seismic effect.

Seismic isolation is an old idea that propose to protect the upper structure by separating it from the damaging movements occur at ground. The history of the isolation systems we use today date back about eight decades. In time, these isolation systems have evolved with technology and became an important subject in civil engineering by providing significant improvements in the earthquake performance of structures.

Different kinds of bearing systems are in use such as Low/High Damping Steel Laminated Elastomeric Bearings, Lead Rubber Bearing and Friction Pendulum Sliding Bearing. The appropriate choice of the bearing type is significant for a successful seismic isolation.

Design and production criteria of bearings have been clarified in American Association of State Highway and Transportation Officials (AASHTO) Specifications. According to these specifications, there are about 15 tests for the bearings or their source materials to satisfy. Some of these tests are as follows:

- ❖ Hardness
- ❖ Shear Modulus
- ❖ Tensile Strength
- ❖ Heat Resistance
- ❖ Ozone Resistance

It's not much clear that whether all these tests are necessary or even related to the actual performance of bearings. On the other hand, among these tests, hardness and shear modulus is the most important two major material properties for elastomeric bearings [2].

## **1.2 Objective of the Thesis**

This study's goal is to investigate steel laminated elastomeric bearings' behavior under continuously aging by applying repetitive back and forth fatigue loadings. The first thing to do to reach that goal is to determine the shear modulus. Shear modulus is the most important material property for the elastomeric bearings and it's calculated according to ASTM D4014 Standard. A very similar method is used for the determination of shear modulus in this study.

After the determination of shear modulus, an answer was sought to determine whether the behavior of elastomeric bearings do change under cyclic horizontal deformations and how the different compression loads will affect this behavior. During the fatigue loading experiments, bearings were compressed under different compression loads (6 MPa, 4.5 MPa and 3 MPa) and forced to make cyclic lateral displacements equal to half of total rubber thickness.

## **1.3 Hypothesis**

This study is important due to the frequent usage of these bearings on earthquake zones and also in very dynamic structures such as bridges and viaducts. Experiments will guide how the behavior of these bearings will be affected over time under dynamic movements.

### GENERAL INFORMATION

#### 2.1 The Concept of Base Isolation

A large proportion of the world's population lives in seismically hazard zones and suffers from earthquakes with miscellaneous magnitude. These earthquakes cause significant life loss and damage to property for years.

Traditionally, buildings were designed to carry the loads on gravity direction. This caused these buildings to be poor conditioned against sudden horizontal deformations. Over time, with the advances at technology and engineering knowledge, earthquake engineering has evolved and some precautions have been innovated to reduce the earthquake's effect on human lives. Countries have started to publish their own national specifications for engineers to follow while designing new structures. These national specifications are always in improvement process with experience and technological advancement.

In conventional approach of designing earthquake resistant structures according to some national code specifications, the building is fixed to the ground by its foundations and it is expected to be damaged under seismic events. The main idea is to build these structures with the sufficient rigidity to carry all the loads properly and resist sudden horizontal displacements. Although this approach satisfies the seismic performance expectations of basic buildings, it is not suitable for critical structures such as hospitals, fire stations, schools, telecommunication centers etc. due to their specific roles during emergency situations. Therefore, base isolation idea has been developed over time.

The modern concept of base isolation date back about eight decades and works by decoupling the upper structure from sub-structure. It is being used to minimize the damages that may occur during earthquake events. The aim is to reduce the transmission of the earthquake loads to the structure by providing horizontal flexibility to the bearings.

If a building could be placed on a perfect frictionless isolation surface, horizontal forces could not be transmitted to the buildings and therefore there would not be any damage at the building. Despite this scenario is out of reality, these bearings still can reduce the transmitted loads greatly.

As can be seen in Figure 2.1, this method also provides reduction of drift in the superstructure. Thus, structural and non-structural elements can be protected from drift-induced damages.

Installation mechanism is the key factor for a successful base isolation. It is very important to have complete understanding of each parameter in the isolation system and their effects on building. Another important point is to supply suitable and flexible non-structural elements such as cables, pipework and any other such systems which cross the base isolator. Elevators and stairs also need special treatment as well.

As the base isolators make great displacements during the ground shaking, a gap needs to be provided around the building to prevent the building hitting the ground. The dimension of this gap depends on seismic hazard zone of the area.

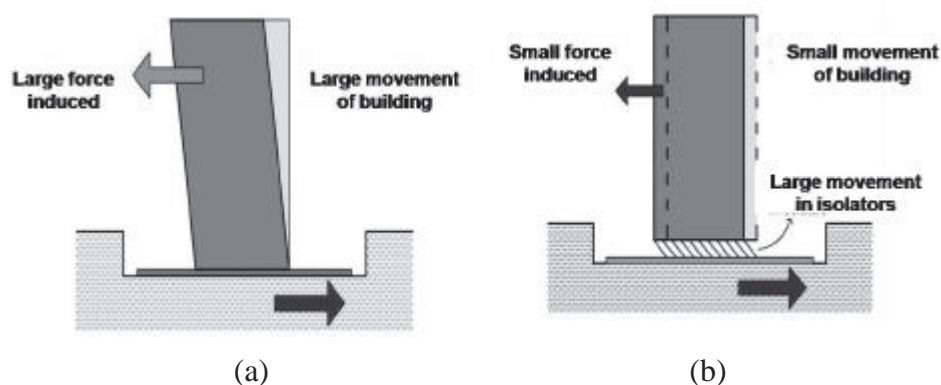


Figure 2.1 Principles of conventional (a) and base isolated (b) structures [3]

Although having the lateral flexibility to move horizontally during an earthquake, the isolation system should have minimum sufficient horizontal resistance to prevent wind-induced movements. Another significant point for these bearings is to have re-centering capability. That means the isolator should return its actual place after the movement and prevent permanent horizontal displacement.

While referring to these isolators' features in horizontal direction, it should not be underestimated that selected isolators should satisfy not only the requirements along the horizontal direction, but also along the vertical direction. Isolators must have sufficient

vertical rigidity in order to transmit vertical loads properly and without having structural damage.

Due to the placement of the building on a horizontally flexible base, effective natural period of the system increases. This situation causes lower acceleration and lower acceleration causes lower forces on building.

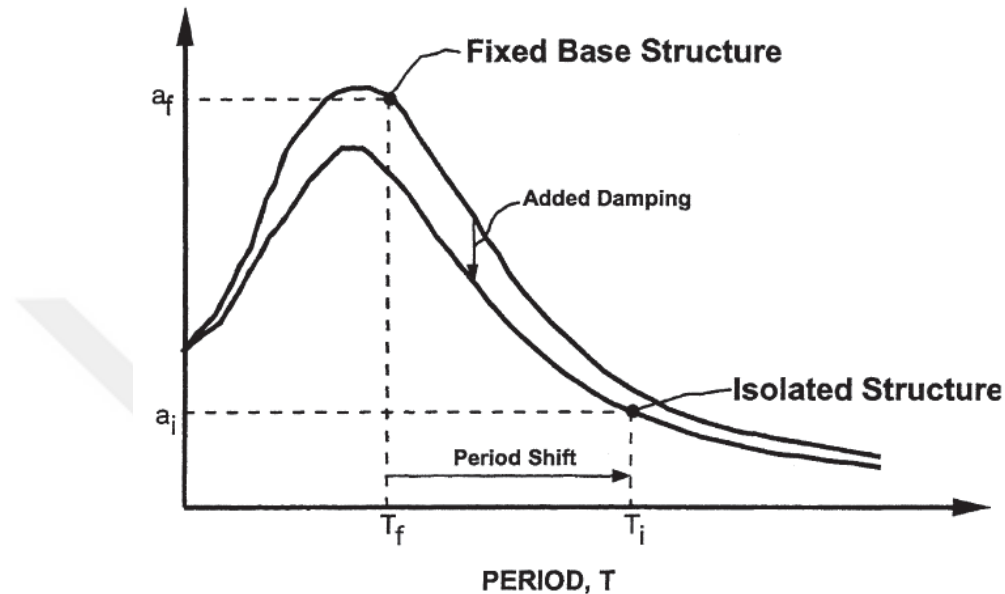


Figure 2.2 Period shift of a structure with base isolation [4]

Base isolation is suitable for structures that have short natural period, such as several stories building on stiff soil. But it is not suitable for structures that have long natural period, such as tall buildings on soft soil.

## 2.2 Common Base Isolators

In this section, the most common types of seismic isolators are explained briefly. These isolation devices can be classified as either elastomeric or sliding. Within the category of elastomeric system, rubber isolators and lead rubber isolators are the two most common devices. Within the sliding system category, friction pendulum system and flat sliding system (with and without re-centering capability) are the most common types. There are also some other protective systems called energy dissipation devices. These devices will be explained later briefly.

Seismic isolation system of a building consists either one type of isolator or a correlation between different types of isolators, or isolators work simultaneously with energy

dissipating devices as a hybrid system. Selection of a suitable isolation system has major role for a successful seismic isolation.

### 2.2.1 Sliding Isolation Systems

While there are different kinds of sliding systems, the most common type is friction pendulum system. These systems tend to decrease the transmission of earthquake-induced forces to the upper structure by using the characteristics of a pendulum. Even some different kinds of this system exist, the main concept of them stays the same: an articulated slider slides on a surface with a certain radius. This radius provides superior re-centering capability compared to rubber bearing or flat sliding bearing. Besides, higher durability and stability are their other advantages.

Friction pendulum isolators can isolate the structure until a predetermined measure of displacement. In Figure 2.3 and 2.4, different stages of a single and triple pendulum bearings and their maximum credible displacements can be seen.

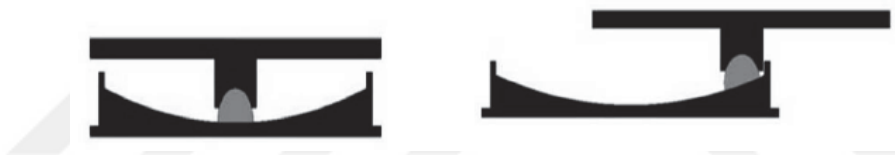


Figure 2.3 Different stages during the displacement of a single pendulum bearing [3]



Figure 2.4 Different stages during the displacement of a triple pendulum bearing [3]

The single pendulum bearing is the first version of these type of bearings. It has a single slider to transmit vertical loads and is more economical to apply. Triple Pendulum Bearing, on the other hand, has three pendulums in one bearing to satisfy different earthquakes that have various strength and frequency.

There is another common base isolator within the category of sliding systems called Flat Sliding System as can be seen in Figure 2.5.

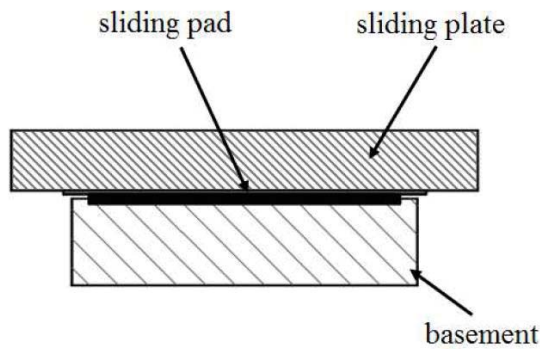


Figure 2.5 Flat sliding bearing system [5]

As mentioned before, re-centering capability of the isolators have significant importance. However, Flat Sliding Bearings have little or no re-centering capabilities. Thus, they are often used with other supportive devices to improve their re-centering capabilities.

### 2.2.2 Elastomeric Isolation Systems

Elastomeric base isolators are one of the most used bearings in the market. These bearings consist of thick rubber blocks bonded with thin steel plates. They have the capability of shear deformation to satisfy lateral movement, the flexibility for rotation in any direction and the vertical stiffness to transmit axial loads properly.

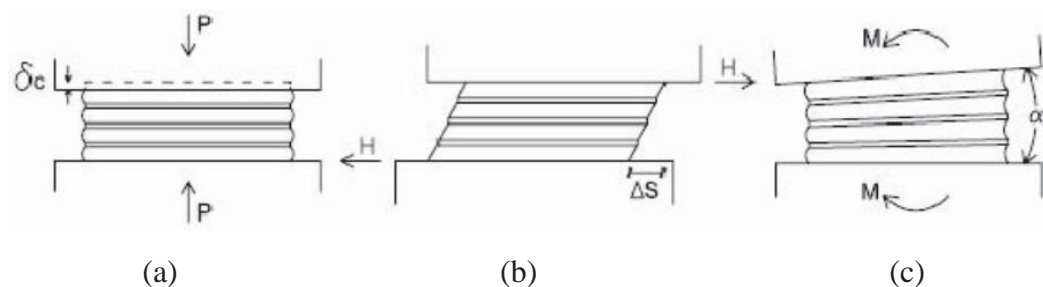


Figure 2.6 Possible deformations of bearings; (a) compression (b) shear (c) rotation [6]

In general, these bearings are made of vulcanized rubber with inner reinforced steel plates. These laminated steel plates contribute axial stiffness to prevent structural damage at isolator due to the tendency to bulge of large rubber blocks.

As can be seen in Figure 2.7, there are two types of elastomeric bearings under this category called steel-laminated elastomeric bearing and lead-rubber bearing.

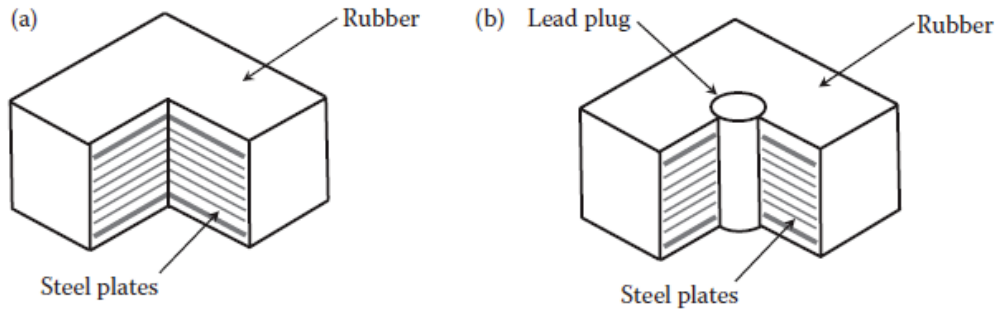


Figure 2.7 Steel-laminated elastomeric bearing (a) and lead-rubber bearing (b) [7]

Depending on the elastomeric materials used, the steel-laminated elastomeric bearings might have either low or high damping capability [8].

Low Damping Elastomeric Bearings have almost linear force-displacement behavior with low damping capability and generally are used with some modifications or assistant devices for energy dissipation.

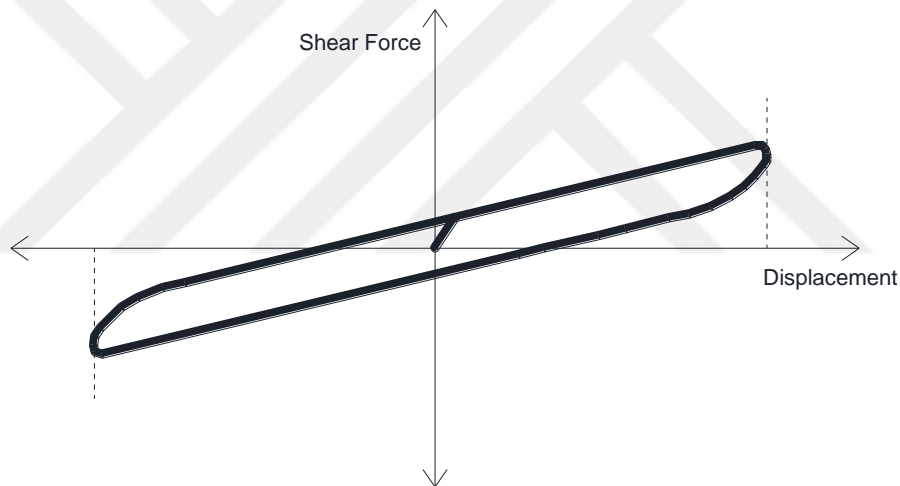


Figure 2.8 Shear force – Displacement behavior of a low-damping elastomeric bearing

However, High Damping Bearings have more nonlinear behavior and the tendency to stiffen under large deformations. Besides, their damping factor is much more superior compared to Low Damping Elastomeric Bearings and they do not need additional tools for energy dissipation.

With the continuous technological advance, these bearings might have damping ratios up to 20% while Low Damping Elastomeric Bearings have 2-3% at 100% strain [5].



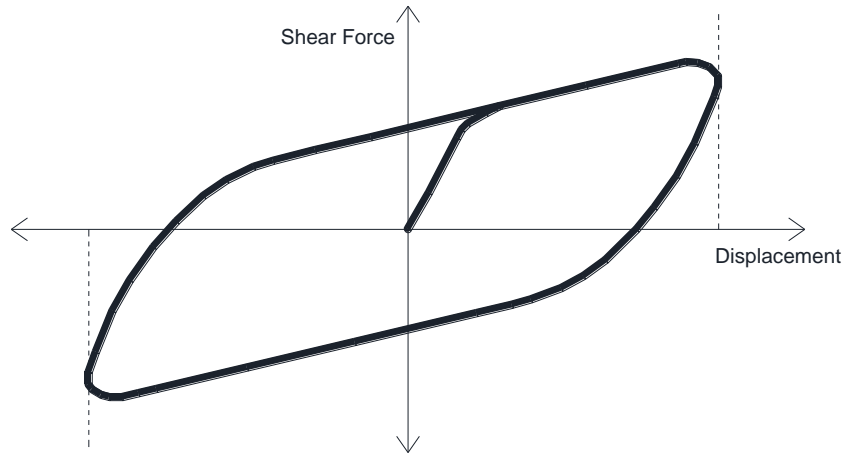


Figure 2.9 Shear force – Displacement behavior of a high-damping elastomeric bearing

Lead Rubber Bearing was invented in New Zealand in 1975 [9]. It can be described as a kind of low-damping bearing that modified with a lead-plug in center. The reason for choosing the lead as a material is because of its unusual behavior under different levels of loading. As mentioned before, isolators have to satisfy sufficient stiffness through horizontal direction to prevent wind-induced permanent displacements. The lead material provides capability of energy dissipation and extra flexibility under earthquake load levels, while providing extra stiffness under service load levels. This mechanical behavior makes lead-rubber bearings the most common type of isolators especially in seismic zones where high level of damping capability is required.

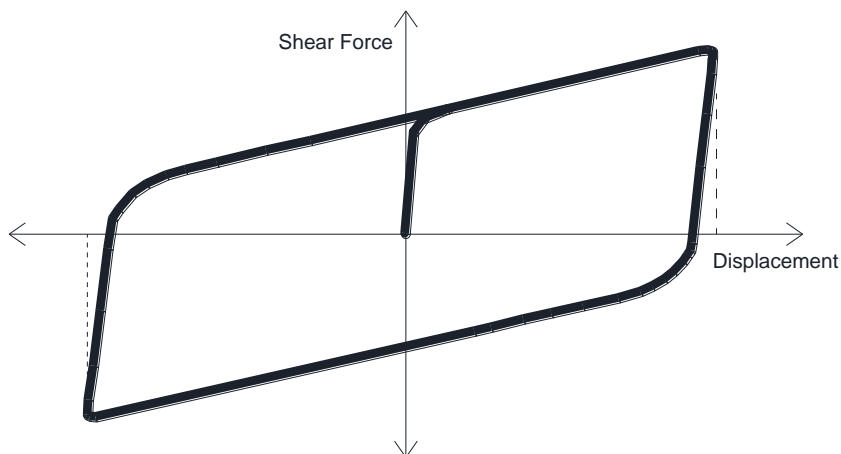


Figure 2.10 Shear force – Displacement behavior of a lead-rubber elastomeric bearing

### 2.3 Energy Dissipation Devices

Although the base isolators described in previous chapter have certain amount of energy dissipation capabilities, additional energy dissipation devices may be required for a better

seismic isolation. These devices do not intercept the earthquake loads from entering the structure. However, they are quite useful to dissipate the energy in different ways and it is common to use energy dissipation systems in a combination with appropriate base isolator systems.

Energy dissipation devices follow the philosophy that the higher damping capability provides lower displacement demand on the structure. Therefore, seismic displacement demand can be met more economically. Placement of these devices on a building has major importance for a successful application. Since these devices are not the main topic in this study, two of the most common energy dissipation devices are explained briefly in this chapter.

*Fluid Viscous Dampers* dissipate the mechanical energy by converting it to heat via high viscous fluid that travels between two internal chambers inside a piston. These devices can dissipate energy even at very small movements and avoid permanent displacements. Due to their effectiveness, these devices are one of the most common type of damping systems [10]. As can be seen in Figure 2.11 below, there are wide variety of installation types to satisfy different load levels, building sizes and shapes.

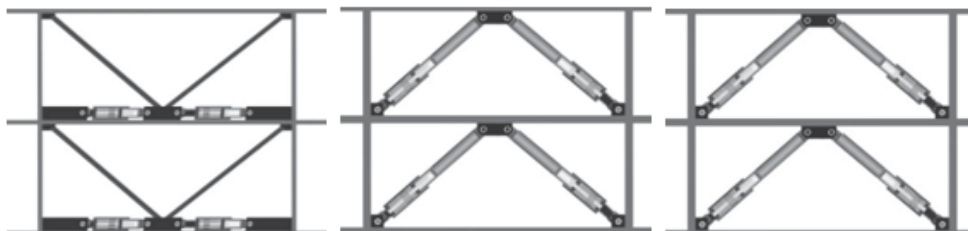


Figure 2.11 Different installation types of fluid viscous dampers

*Friction Dampers* convert the mechanical energy into heat via mechanical friction between the damper and metal or other surfaces that separated by friction pad material. They are mostly used in moment-frames and diagonal braces [3].

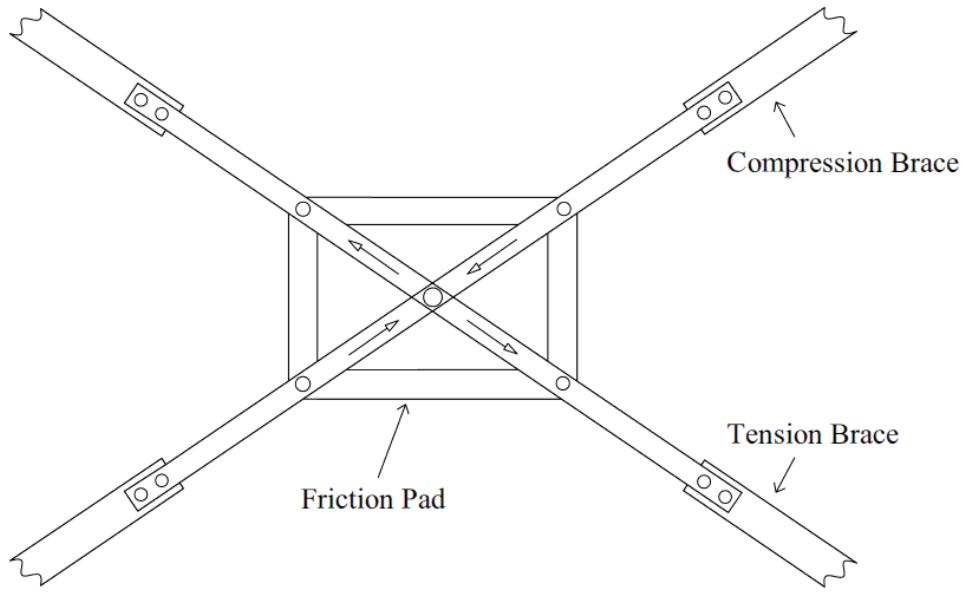


Figure 2.12 Pall frictional damper [11]

### STEEL-LAMINATED ELASTOMERIC BEARINGS

Since the steel-laminated elastomeric bearings were used for experimental studies, some detailed information about these bearings were clarified in this chapter.

Elastomeric bearings have been used since 1950s. They are effective and economical especially considering the problems that may occur during an earthquake. As explained before, Steel Laminated Elastomeric Bearings can have either low or high damping capability related to the elastomer material used during the manufacturing process. In a relation to the chosen type of isolator, some additional tools (like energy dissipation systems) or structural elements might be necessary to provide sufficient damping capability to the structure.

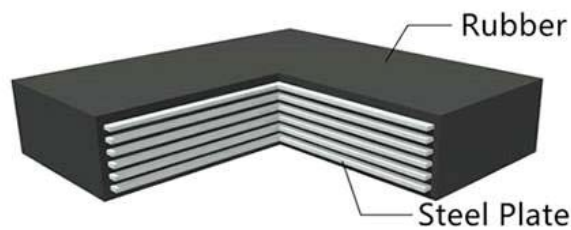


Figure 3.1 Steel-laminated elastomeric bearing [12]

Elastomers can be defined as highly nonlinear, hyperelastic and nearly incompressible ( $\nu \approx 0.5$ ) materials. Linear elastic isotropic materials can be described by constants such as Young's Modulus ( $E$ ), Shear Modulus ( $G$ ), Bulk Modulus, ( $K$ ) and Poisson's Ratio ( $\nu$ ). Unlike linear elastic isotropic materials, hyperelastic materials have time dependent, nonlinear and changeable stress-strain relationship.

Because the manufacturing process has significant importance as much as workmanship for a successful application, some test requirements are clarified for elastomeric bearings

in AASHTO M251-06, *Standard Specification for Plain and Laminated Elastomeric Bridge Bearings* to prevent performance issues and ensure a certain level of performance.

Although having wide range of test requirements for elastomeric bearings, it is not completely clear whether all these tests are required or even related with the actual performance of a bearing. For general, hardness and shear modulus are the most essential and major material properties for elastomeric bearings [2]. However, it shouldn't be underestimated that the compression stiffness has also a major significance since the bearing has to transmit axial loads properly. These terms and their place in related specifications are clarified in following sections.

### 3.1 Compression Stiffness

Sufficient axial stiffness of an elastomeric bearing is provided by laminated steel layers. Although these layers have nearly no effect to lateral stiffness or flexibility, they are essential to provide the sufficient axial stiffness in order to carry and transmit vertical loads properly. Since the elastomer materials are almost incompressible ( $\nu \approx 0.5$ ), they have tendency to expand laterally under compression loading due to the Poisson effect.

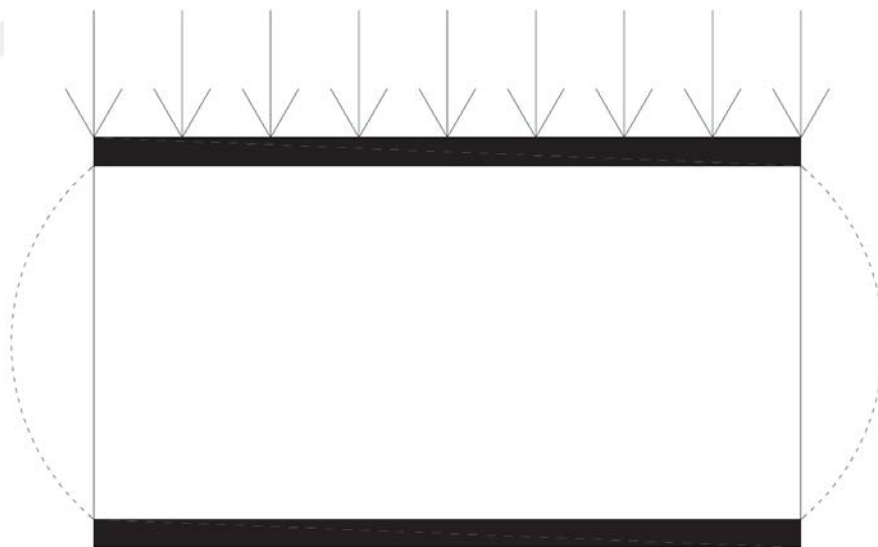


Figure 3.2 Bulging effect

As Figure 3.2, assuming an elastomeric bearing without sufficient amount of steel layer plates, suffer structural damages and disorders that lead to serious performance issues no matter how lateral features were well-conditioned. If no precautions are taken, the bulging cause higher shear stresses at the contact area between elastomer and steel layers that

eventually lead to shear failure. This undesirable situation is one of the most common failure types for steel-laminated elastomeric bearings and it needs serious consideration. Properly placed steel layers are the key factor to provide sufficient axial stiffness to the bearing. Assuming two elastomeric bearings with different amount of inner steel plates.

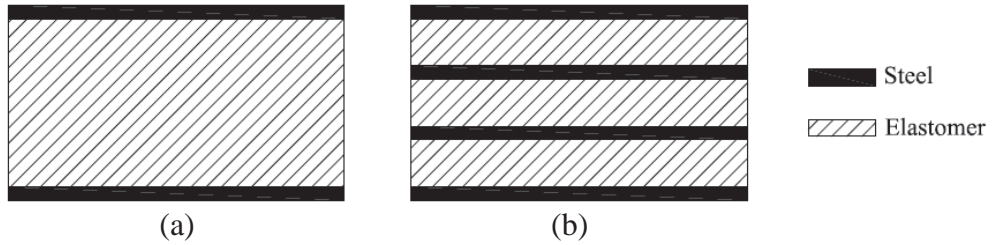


Figure 3.3 Section views of elastomeric bearings with different inner layers

The total equivalent stiffness of these different type of elastomeric bearings can be represented as:

for Type-a:

$$\frac{1}{K_a} = \frac{1}{K_{s1}} + \frac{1}{K_e} + \frac{1}{K_{s2}} \quad (3.1)$$

for Type-b:

$$\frac{1}{K_b} = \frac{1}{K_{s1}} + \frac{1}{K_{e1}} + \frac{1}{K_{s2}} + \frac{1}{K_{e2}} + \frac{1}{K_{s3}} + \frac{1}{K_{e3}} + \frac{1}{K_{s4}} \quad (3.2)$$

Where:

$K_a$  → Equivalent axial stiffness of bearing type-a

$K_b$  → Equivalent axial stiffness of bearing type-b

$K_{ei}$  → Equivalent axial stiffness of elastomer layer

$K_{si}$  → Equivalent axial stiffness of steel layer

Since the steel material has much more superior stiffness compared to elastomer material ( $K_s \gg K_e$ ), it can be observed from these two equations that equivalent axial stiffness of bearing type-b ( $K_b$ ) is higher than type-a ( $K_a$ ).

However, due to the tendency of bulge of elastomer materials, finding out the equivalent axial stiffness is not the only criteria for adequate axial performance. If it was, there would not be any need to place the steel materials in different layers and it would be enough to

use sum of their thickness in one or two layers. But in this case, the area under bulge effect would remain the same.

Laminated steel layers inside the bearing partially prevent the elastomers from bulging. The main idea for using laminated steel layer is to decrease the area of bulge.

The determining term about the bulging is shape factor. Shape factor can be described as the ratio of compression load area to bulge area. That means, for a rectangular bearing without a hole:

$$S_i = \frac{L_1 \times L_2}{2 \times h_i \times (L_1 + L_2)} \quad (3.3)$$

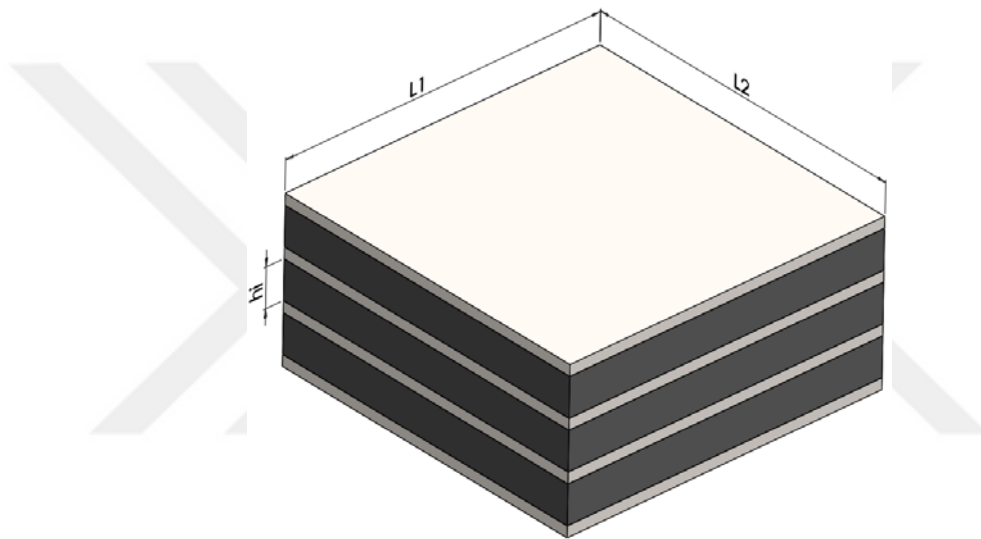


Figure 3.4 3D view of a bearing

where:

$S_i$  → Shape factor of the  $i$ th elastomer

$L$  → Plan dimension of the bearing

$h_i$  → Thickness of the  $i$ th layer

In Figure 3.5, deformed shapes of the two different type of elastomeric bearings can be seen. Both have 100 mm square plan dimensions. The bearing on the left has 42 mm rubber block between 2 x 8 mm steel plates and the bearing on the right has 3 x 14 mm rubber blocks between 4 x 4 mm steel plates. Shape factor of these bearings are determined as 0.60 and 1.80, respectively.

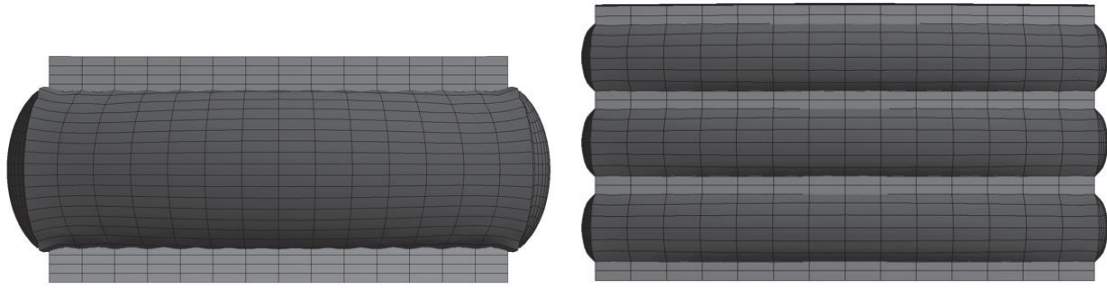


Figure 3.5 Bearings with different inner layers under same compression load

As the result of the finite element analysis of these bearings, it is clear that the bearing without inner laminated steel layers has suffered much more deformation compared to the other bearing under same compression load. During the design process of a structure, the deformations of these bearings are limited. Thus, lower deformation means higher load capacity.

To get actual knowledge about elastomeric bearings' behavior under compression loading, a procedure called *Compression Stiffness Test Method* is clarified in *AASHTO M251-06*.

According to this specification, a pair of elastomer material block sandwiched between rigid plates are tested under cyclic loading in certain environmental conditions. The test is executed under the period within the range of 30-120 seconds and the specimens are forced to make displacement equal to 10 percent of total elastomer thickness.

The Force-Displacement graph that obtained during the test process is used for the determination of compression stiffness. For the third cycle, the values are measured for every 1 percent increment of the displacement and a best-fit straight line is drew. Finally, the compression stiffness is found from the equation:

$$E_s = K_1 \frac{2T}{A} \quad (3.4)$$

where:

$K_1$  → The slope of the straight line

$T$  → Average elastomer thickness

$A$  → Plan area



### 3.2 Hardness

As mentioned in previous chapters, elastomeric bearings get their flexible features from the vulcanized rubber layers. Vulcanization is a chemical process to improve the mechanical properties of natural or synthetic rubbers. This method was discovered by Charles Goodyear in the year 1839. Vulcanized rubber is stronger and more rigid than the natural rubber. However, it still has the elasticity to stretch reversibly. This kind of polymers are called elastomers. The quality of elastomer material has a significant role on the behavior of a bearing. For use in elastomeric bearings, vulcanized rubber layers should be either natural rubber or chloroprene rubber, but no reclaimed rubber can be used [13].

When it comes to specify the behavior of an elastomer, hardness is one of the most important material properties. Hardness can be described as the resistance to elastic indentation as measured under specified conditions. Two common test methods are clarified for the determination of the hardness in *ASTM* standards.

The durometer hardness is commonly referred to as the Shore hardness and it was being used to specify the elastomer material type until 1985 [2]. The measurement device - durometer- has a needle on a spring protruding from the end. The gauge is forced as much as it can go and the needle indicate corresponding hardness measurement [14]. This method covers twelve types of rubber durometer hardness measurement devices: Types A, B, C, D, DO, E, M, O, OO, OOO, OOO-S and R [15]. Materials like soft vulcanized rubber, natural rubber, elastomers, nitriles etc. have the shore hardness between 20 and 90 and they are measured with Type A durometer device [16]. Generally, the Durometer Hardness for steel laminated bearings should be in range between 50A to 70A.

International Rubber Hardness Degrees (IRHD) is an alternative common test method for the determination of hardness of the vulcanized rubber. The instrument has a spherical indenter which indents the sample under a minor and major load. IRHD degrees is measured by the differential indentation depth [17]. The correlation between displacement and IRHD degrees are published in *ISO 48* standard.

### 3.3 Shear Modulus

Until 1985, the durometer hardness was the material property that had been used to define the behavior of an elastomer. However, in 1980s, shear modulus was strongly suggested to be specified for elastomeric bearings [18] [19]. The reason behind this idea is the weak correlation between hardness and stress-strain relationship along shear direction. Shear modulus is a material property to define stress-strain relationship in shear direction and it provides deeper understanding about the lateral behavior of a bearing compared to hardness. Since the lateral features are significant considering the reason to use these bearings, the determination of shear modulus has provided the predictions to be more accurate.

Although there is a slight relation between the hardness and shear modulus, elastomers with same hardness might have different shear modulus. Especially if the bearings were bought from different manufacturer, shear modulus can differ greatly as a result of vulcanization process even if the hardness scale is the same. Estimated shear modulus must fall within the specified ranges [2].

Table 3.1 Relation between IRHD and shear modulus for elastomers [20]

Hardness (IRHD( $\pm 2$ ))	35	40	45	50	55	60	65	70	75
Shear Modulus(G), MPa	0.38	0.45	0.53	0.63	0.75	0.89	1.04	1.22	1.42
Bulk Modulus( $E_b$ ), MPa	2000	2000	2030	2060	2090	2120	2150	2180	2210

Table 3.2 Relation between shore A durometer and shear modulus for elastomers [21]

	Hardness (Shore A)		
	50	60	70
Shear Modulus (MPa) @ 23°C	0.66-0.90	0.90-1.38	1.38-2.07

Two kinds of experimental studies were clarified for the determination of shear modulus. These tests are named as Inclined Compression Test [22] and Quad Shear Test [13].

*Inclined Compression Test Method* is typically executed with a pair of full-size elastomeric bearings. Bearings are located between three inclined platens and forced to 65 percent strain under compression load.

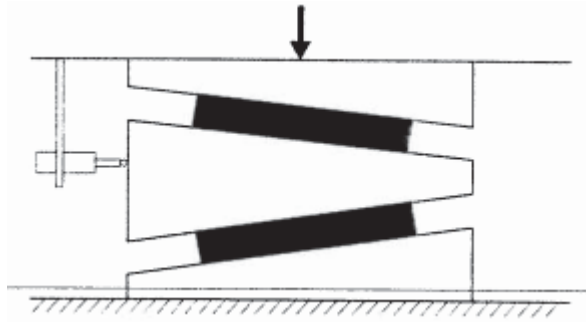


Figure 3.6 Inclined compressive test set-up [22]

During the experiment, four successive loading and release cycles are carried out under the period of 4-6 minutes for per cycle. The 4<sup>th</sup> cycle is used for the determination of shear modulus.

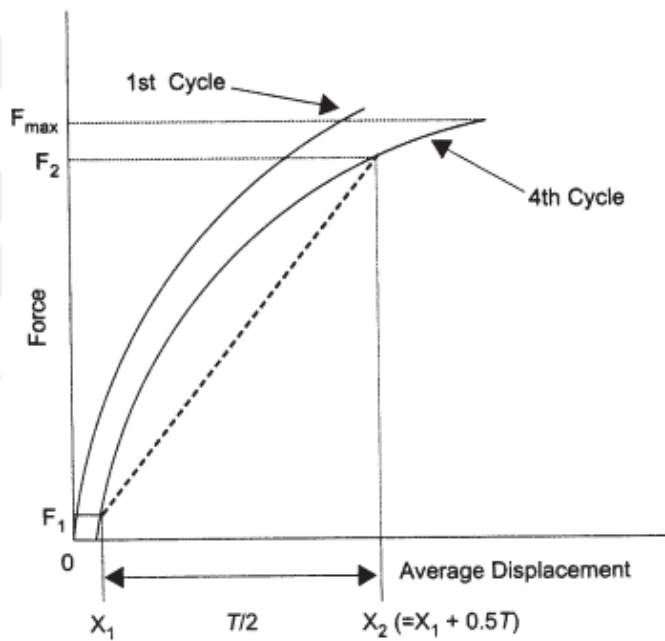


Figure 3.7 Inclined compressive test stress-strain graph [22]

In this graph,  $F_1$  is taken as an effective origin with a value of 5 kN or two percent of the maximum load on fourth cycle, whichever is smaller.  $X_1$  is found as the extension of  $F_1$ .  $X_2$  is calculated as  $X_1 + 0.5T$ , where  $T$  is the total elastomer thickness.  $F_2$  is found as the extension of  $X_2$ . Finally, when all unknown parameters are found, the shear modulus is calculated as follows:

$$\text{Shear Modulus} = 2 (F_2 - F_1) / (A \times n) \quad (3.5)$$

$n \rightarrow$  The factor to convert vertical load to horizontal load

Although the Inclined Compression Test Method is more realistic, it's much more costly compared to Quad Shear Test Method.

*Quad Shear Test Method* is clarified in ASTM D4014-03 standard. According to this method, small bearing samples cut from the full-size bearing are bonded to the rigid plates with a suitable bonding system. After the preparation of test set-up, the middle plate is forced to a deformation equal to the rubber thickness under the period of 30-60 seconds.

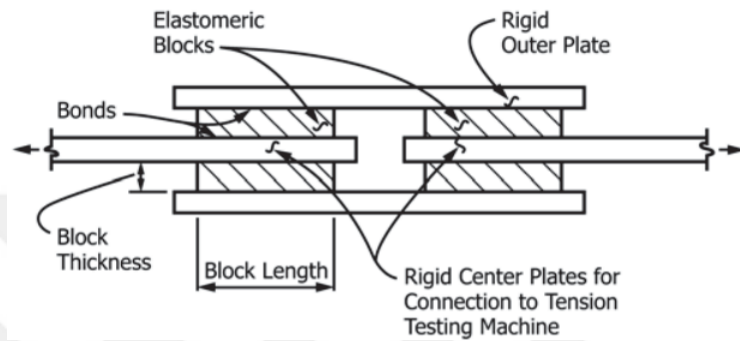


Figure 3.8 Quad shear test set-up [13]

After the five successive loading and release cycles, shear modulus is determined by using the stress-displacement curve that occurs during the sixth cycle.

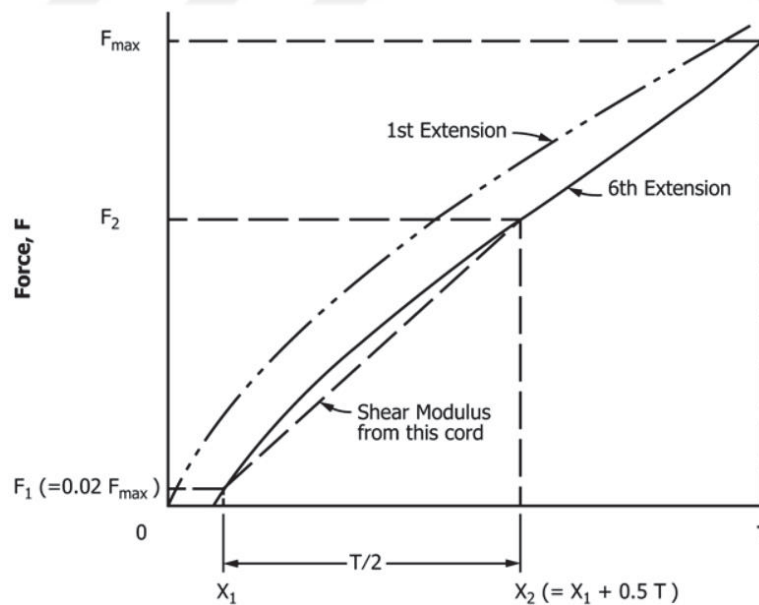


Figure 3.9 Quad shear test stress-strain graph [13]

In this graph,  $F_1$  is taken as an effective origin calculated as two percent of the maximum load on sixth cycle.  $X_1$  is found as the extension of  $F_1$ .  $X_2$  is calculated as  $X_1 + 0.5T$ , where  $T$  is the total elastomer thickness. As the last,  $F_2$  is found as the extension of  $X_2$ .

Finally, when all unknown parameters are found, the shear modulus is determined as follows:

$$\text{Shear modulus} = 2 (F_2 - F_1) / A \quad (3.6)$$

In this study, the shear modulus is determined with a method very similar to Quad Shear Test Method.



## CHAPTER 4

---

### EXPERIMENTAL STUDIES

In this section, some of elastomeric bearing samples cut from the original bearing are going to be used for experimental studies in order to get complete knowledge about their behaviors and mechanical properties under different certain circumstances. These tests also assist to identify whether the boundary conditions are satisfied for the manufacturing process or to define material properties for computer-aided analysis.

Bearing samples have 100 mm x 100 mm plan dimensions and 62 mm total thickness consists of 3 rubber and 4 steel layers. The total rubber thickness is 42 mm.

Instron 8803 Fatigue Testing Systems were used during the experiments. This system has 500 kN static and dynamic load capacity under maximum 207 bar pressure. This allows us to affect dynamic loads on samples under certain frequency properly.



Figure 4.1 Instron 8803 Fatigue Testing System

Composite materials generally have the physical properties of the materials that compose them. For elastomeric bearings, the bearing has the flexibility in lateral direction to satisfy ground movement and in the meantime, it has the rigidity to prevent wind-induced movements and carry the vertical loads properly.

Carrying the vertical loads without structural damage at the bearing, especially with the consideration of the eccentricity that could take a place during the earthquake movements, is directly related with compression stiffness and has a vital importance for the upper structure.

Determination of the compression stiffness is clarified in *AASHTO* as mentioned before. According to the specification, three loading and release cycles are carried out to a pair of bearing samples until reaching the 10 percent of total rubber thickness under specified frequency. After, the compression stiffness is determined via the stress-strain graph that obtained during the third cycle.

In this study, however, the cyclic loading could not be executed for the determination of compression stiffness due to the lack of time. Instead, the specimen had been forced to make deformation until the structural failure occurs.

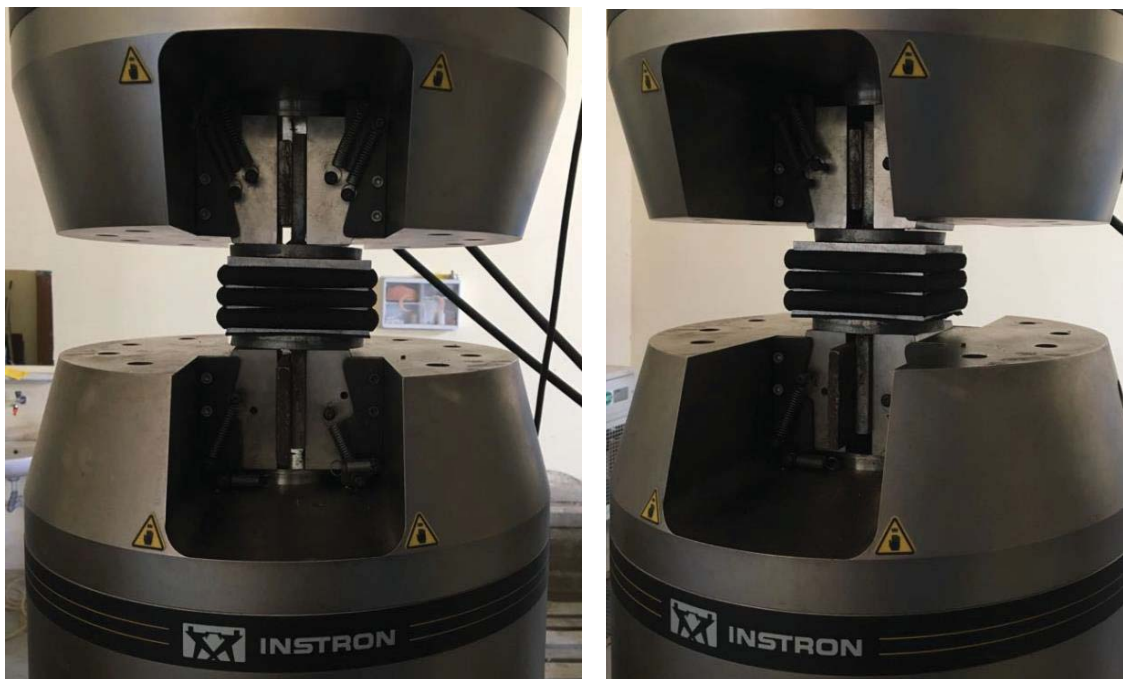


Figure 4.2 Compression loading

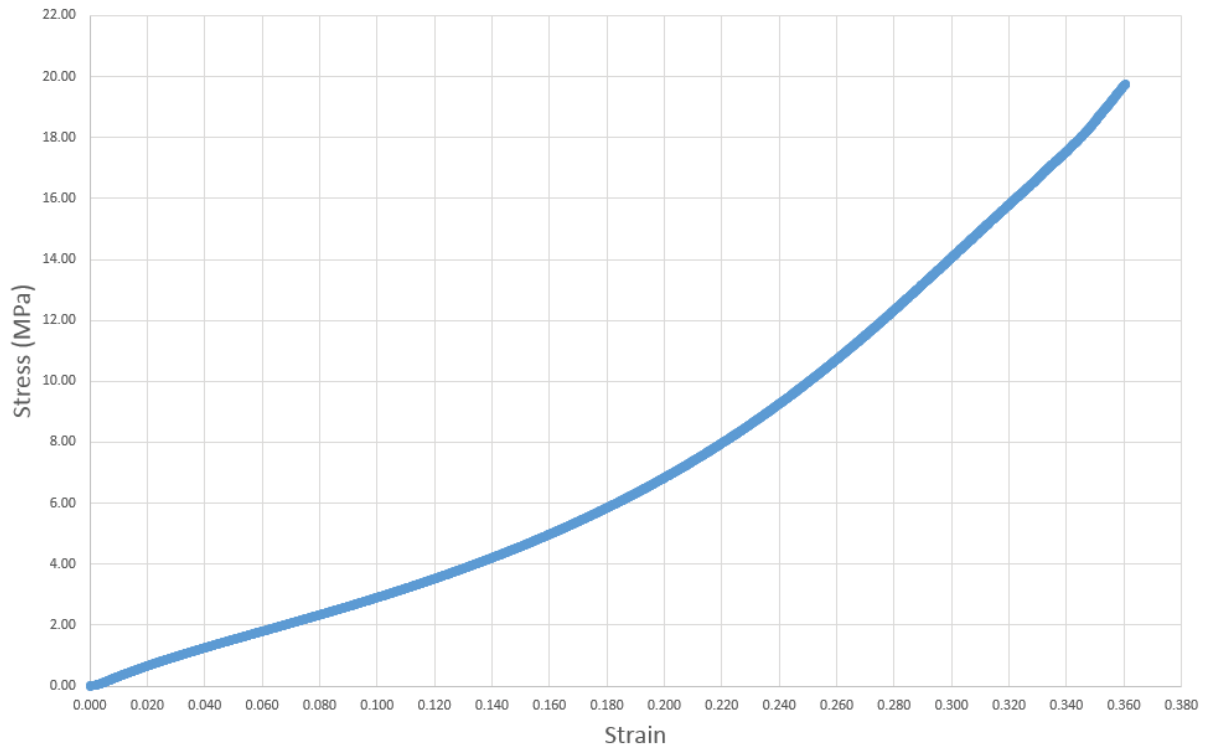


Figure 4.3 Stress-Strain graph under compression loading

Above, the stress-strain graph until the 36 percent strain level can be observed. As having 42 mm total rubber thickness, that means 15.12 mm total axial deformation. After this level of strain, a bonding failure between the rubber blocks and steel plates started to appear at bulging areas.

As expected, due to the hyperelastic material behavior of elastomer rubber blocks, a nonlinear stress-strain graph is obtained. Although there is a nearly linear behavior at the beginning, the material became stiffer as it was compressed more.

One of the main ideas behind the usage of the low strain levels for the determination of compression stiffness in specifications might be this material behavior that gets stiffer in time under increasing compression stress. Since the bearing may suffer some structural damages under high strain levels -as happened in this experiment-, it is important to ensure the bearings have the sufficient stiffness that prevents high deformations under service loads.



Considering the AASHTO M251-06, the strain levels between 0.00 and 0.10 are illustrated below.

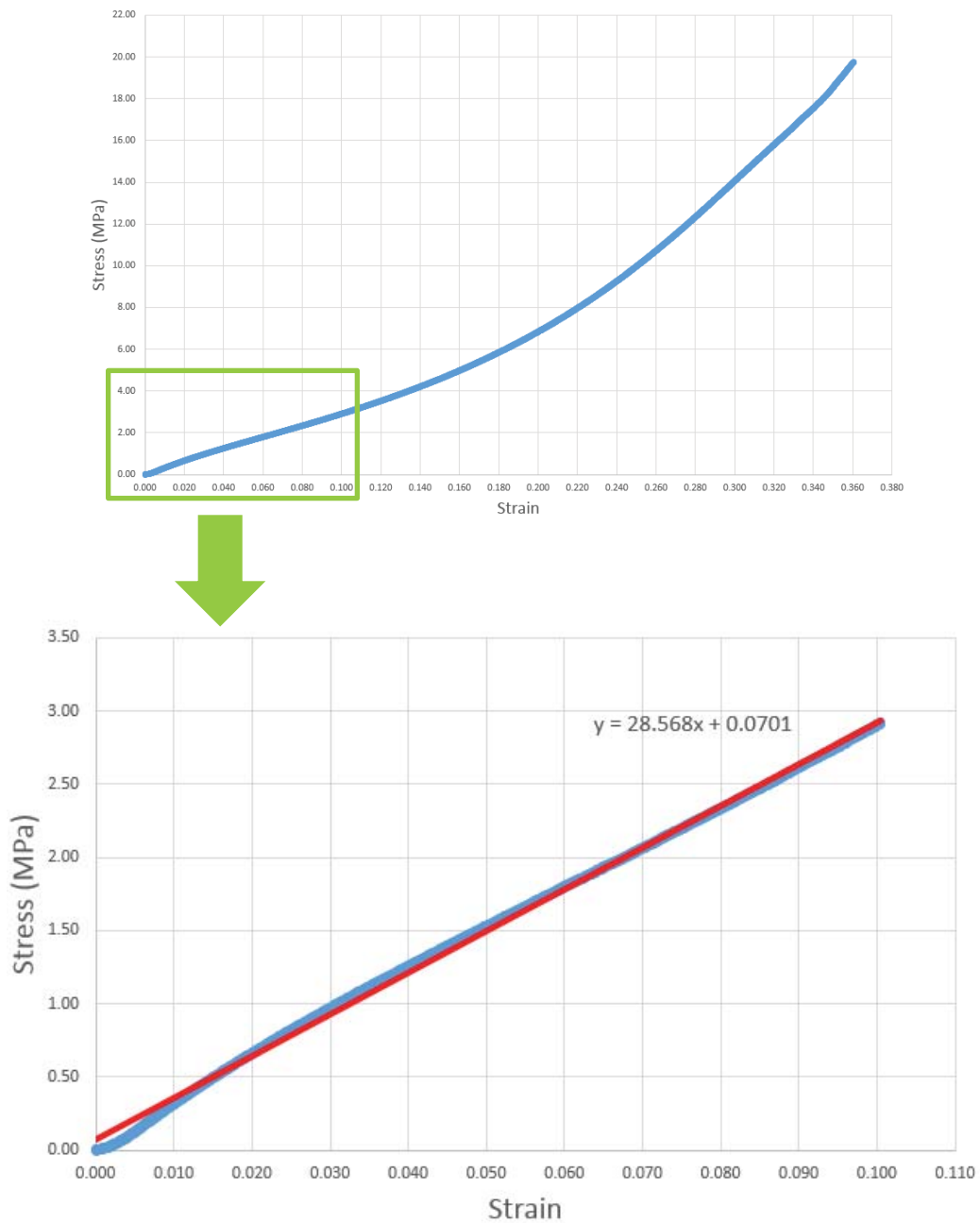


Figure 4.4 Stress-Strain graph under compression loading (low strain levels)

It can be observed that the relation between stress and strain is quite linear since the best-fit straight line is mostly interfere with the graph. The formula of this straight line is:

$$y = 28.568x + 0.0701$$

From the slope of this straight line, the compressive modulus,  $E_s$ , can be found.

$$E_s = 28.6 \text{ MPa}$$

To see the dramatic increase at stiffness, the higher strain levels were scoped out below.

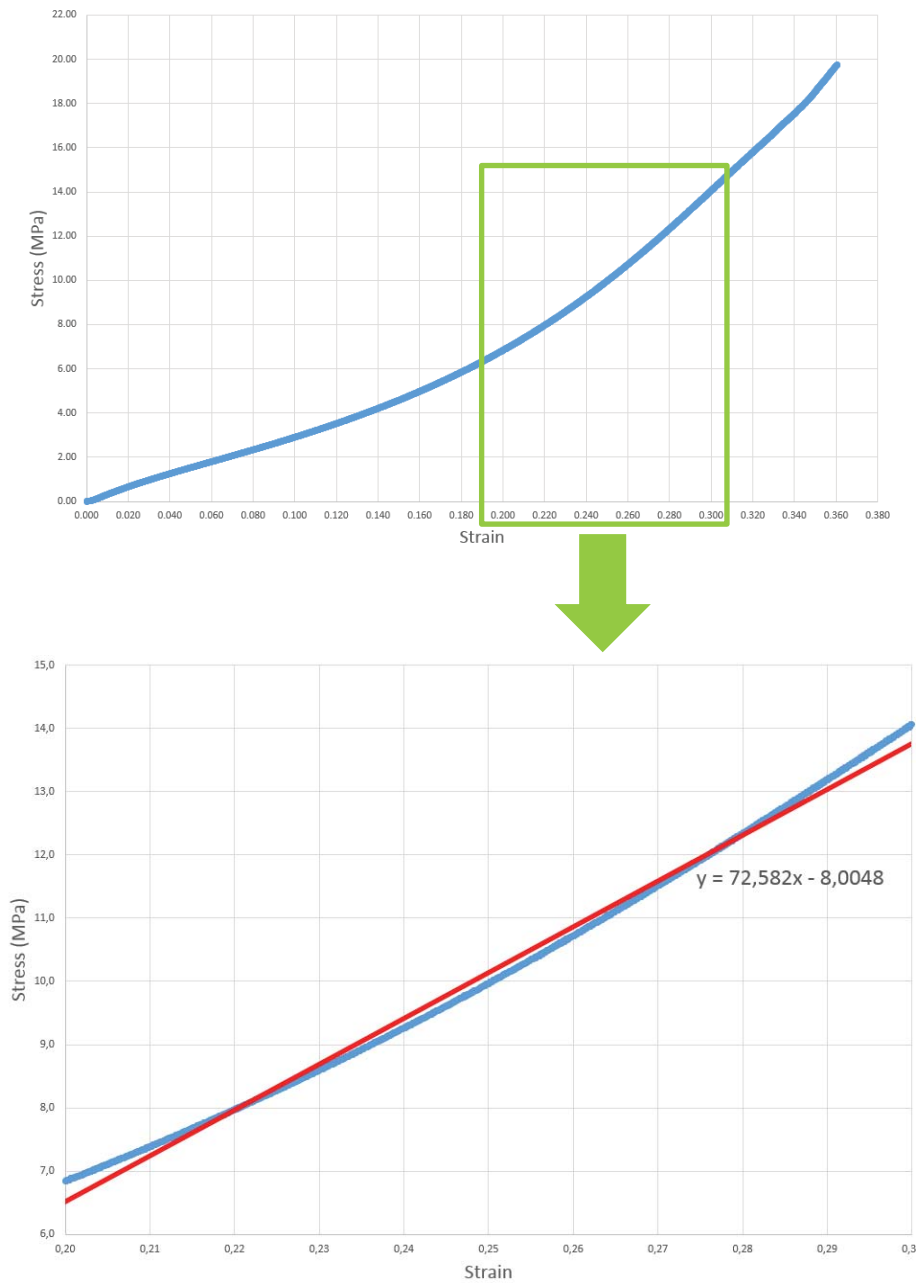


Figure 4.5 Stress-Strain graph under compression loading (high strain levels)

As can be seen above, between the strain values of 0.2-0.3, the compressive modulus is found as 72.6 MPa. That indicates the significant increase –almost 2.5 times– of compression stiffness at higher levels of strain. Although this nonlinear behavior might be used for the computer-aided analysis, however, it is safer to assume the material continues its linear, low stiff behavior through the higher strain levels since these bearings are generally used for the structures with strategic importance.

#### 4.1 Determination of the Shear Modulus

As explained in previous chapters, shear modulus is one of the most important material properties for elastomeric bearings and there are two test set-ups for the determination of shear modulus according to *AASHTO* Specifications. Inclined shear test method is executed with full size bearings. The quad shear test method however, is clarified in *ASTM D4014-03* and executed with two pairs of bearing samples cut from the full-size bearing. According to quad shear test method, a pair of bearing samples were cold bonded to three steel plates. Contact surfaces were cleared with neutralizer before the glue with high shear strength was used to bond the bearing and steel plates. Two of these steel plates were constant, while the middle one was forced to make displacement equal to half of the total rubber thickness.

In this study, a method close to quad shear test method was followed. A pair of elastomeric bearing and a steel part for the lateral load application were used for the experiment.



Figure 4.6 Steel parts used for the determination of shear modulus

The steel part was manufactured based on the bearing's dimensions. As it will be seen in following pages, the steel plate on the right side is the fixation part of the system. The bearings are placed between the two plates on left side and another plate between the bearings provide the lateral movement.



Figure 4.7 Test set-up

The test set-up with Instron 8803 Fatigue Loading System can be seen above. As explained, the bottom part is the fixation point, while the upper part placed between two bearings is for the application of movement along shear direction.



Figure 4.8 Deformation along shear direction

It should be checked if there is any kind of failure on the bearings during the experiment. ASTM Standard clarifies that if there are any failure on the bearing (slip of the blocks, bond failure etc.), the test specimen should be prepared again and the experiment should be repeated in such circumstances.

The bearings were forced to make displacements equal to total rubber thickness of one bearing (half of total rubber thickness). Same as the ASTM D4014-03 standard clarifies, six successive loading and release cycles were carried out under 0.025 Hz frequency.

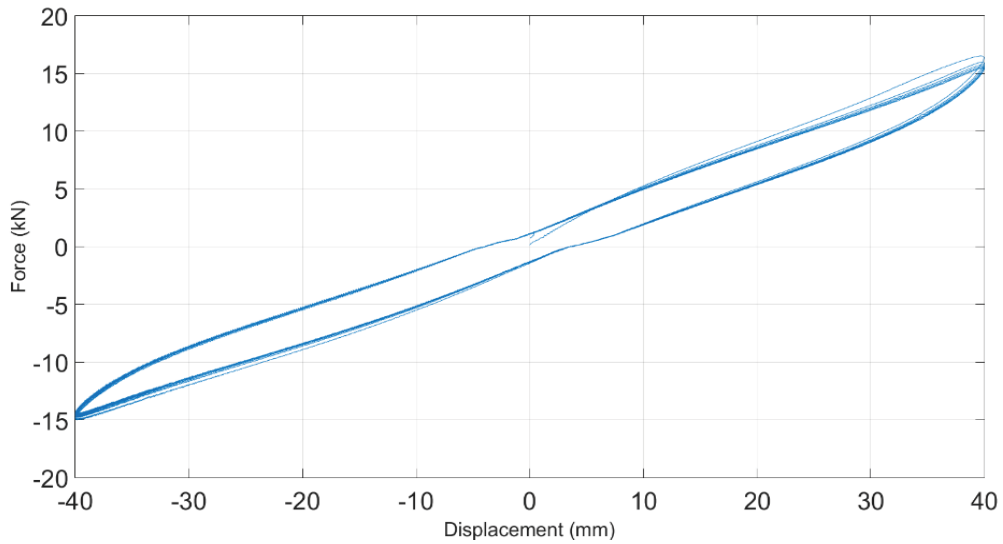


Figure 4.9 Hysteresis loop obtained from five cycles

Since the first five cycles are carried out in order to stabilize the stress-strain behavior of the system, the stress-strain graph obtained during the sixth cycle were used for the determination of shear modulus.

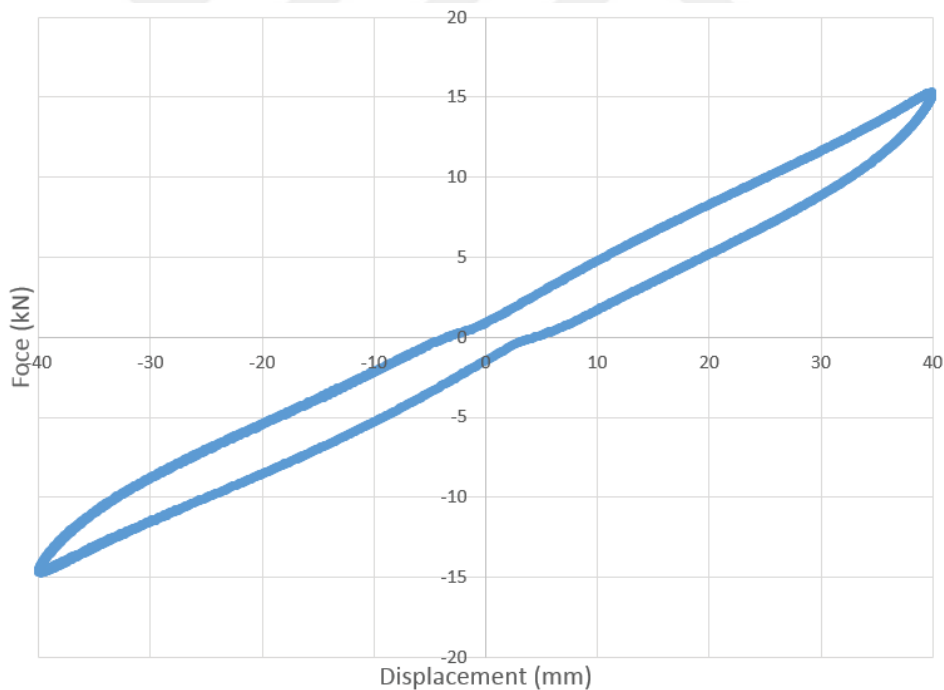


Figure 4.10 Hysteresis loop obtained from only the sixth cycle

The calculation formula for the determination of shear modulus is as follows:

$$\text{Shear modulus} = 2 (F_2 - F_1) / A \quad (4.1)$$

While A is the cross-sectional area,  $F_1$  and  $F_2$  values are obtained from the sixth cycle. ASTM standard clarifies how to get these values.

As first, the maximum force in the sixth cycle,  $F_{max}$ , was found as 15.3 kN. Effective origin  $F_1$  is %2 of  $F_{max}$ , and its extension was found as  $X_1$ .  $X_2$  was calculated as  $X_1+0.5T$ , where  $T$  is the average rubber block thickness. After  $X_2$  was calculated,  $F_2$  was found from its extension. Below, a required piece of the graph can be seen.

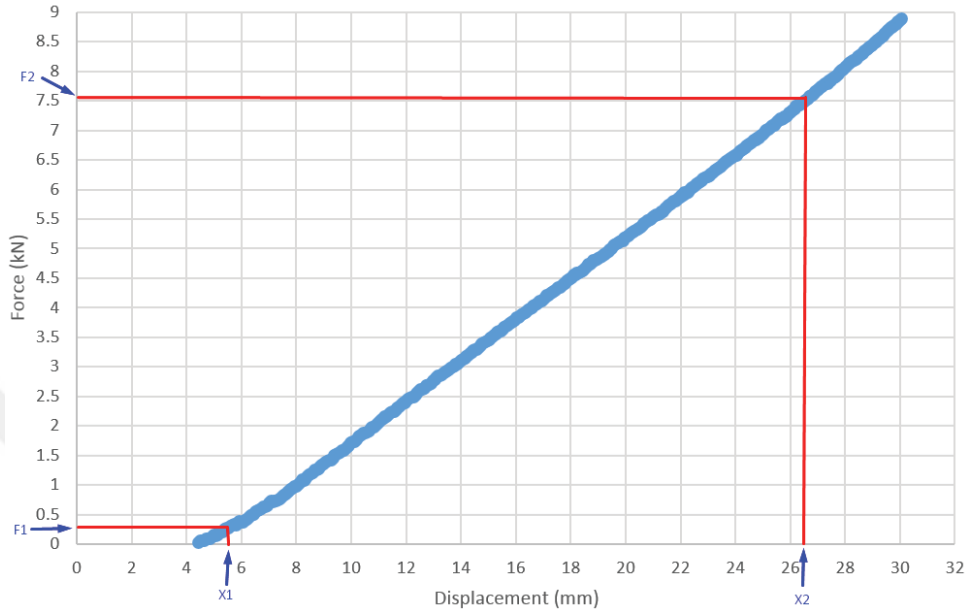


Figure 4.11 Values for the determination of shear modulus

To summarize, the values emphasized above were found as:

$$F_1 = 0.02 \times 15.3 \text{ kN} \rightarrow 0.306 \text{ kN}$$

$$X_1 \rightarrow \text{The extension of } F_1 \rightarrow 5.55 \text{ mm}$$

$$X_2 \rightarrow X_1 + (T/2) \rightarrow 5.55 \text{ mm} + (42 \text{ mm} / 2) \rightarrow 26.55 \text{ mm}$$

$$F_2 \rightarrow \text{The extension of } X_2 \rightarrow 7.52 \text{ kN}$$

Once the values are obtained, shear modulus of the bearing is calculated as:

$$\text{Shear modulus} = 2(7520 \text{ N} - 306 \text{ N}) / (100 \text{ mm} \times 100 \text{ mm}) = 1.44 \text{ MPa} \quad (4.2)$$

## 4.2 Shear Stiffness under Different Pressure Loading

The bearing samples were not axially forced during the determination of shear modulus. However, in practical, these bearings are under considerable amount of axial load and this situation may cause significant change at shear stiffness since these properties are related because of the material behavior. The objective of this experiment is to get information about elastomeric bearings' lateral behavior under various pressure loading.

For the experiment, a different but similar steel part that is more suitable to apply the compressive load was used.



Figure 4.12 Steel parts used for the experiment

In order to stimulate the axial load and shear deformation on the same system, a different but similar steel parts (above) were used. On the right side, there is the second part that transmits the axial loads to the bearing samples and it is placed at the very top of the bearings. The shear deformation is applied as explained in previous chapter.

Before the preparation of test set-up, the contact surfaces between the bearings and steel parts should be cleared with neutralizer before each experiment in order to provide sufficient bonding effect between the materials. After the preparation of the materials, each part and bearings are placed properly. The bearing samples are grouped depending on the axial pressure on them, which are 3, 4.5 and 6 MPa.

The experiment consists of two phases. The first phase is to apply the axial load before the horizontal movement which is executed in phase two. In order to keep axially deformed situation after the first stage, the system is modified with additional steel parts as below.



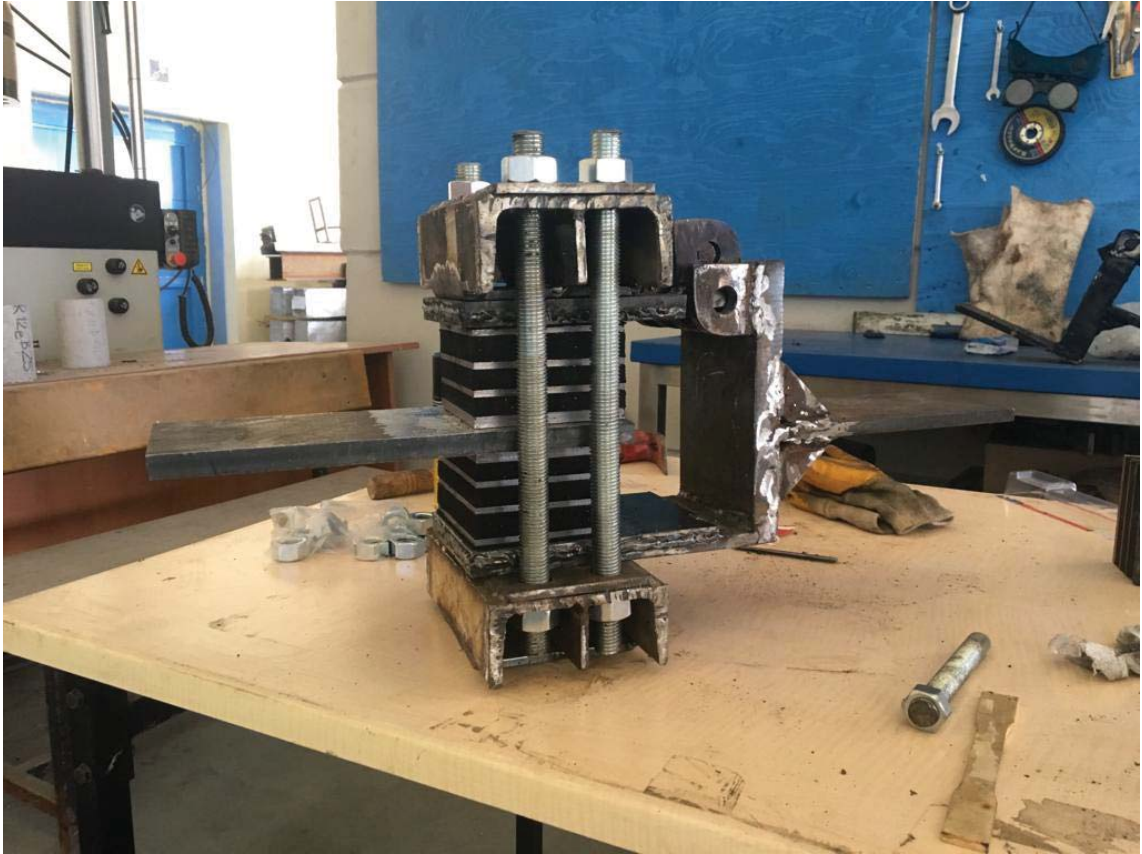


Figure 4.13 Preparation for the experiment

The additional parts placed at the very top and bottom of the bearings. These parts provide the transmission of axial loads.

Below, the ultimate set-up for the phase one can be seen.



Figure 4.14 Test set-up for phase one

In order to prevent the system from releasing after the first phase, four pieces of rods are going through these parts. The nuts are squeezed at the end of the first phase, thus the axial load on the system stays still.

During the experiment, the samples should be checked whether there is any failure on samples. For instance, a bonding failure occurred on a bearing which is under 6 MPa pressure. The experiment should be repeated with new samples in such circumstances.



Figure 4.15 Bonding Failure during the first phase

After the first phase is completed and the nuts are squeezed, the bearings are ready for the lateral movement.



Figure 4.16 Squeezing the nuts after the first phase

The experiment continues with the second phase in case of the samples are passed the first phase without any failure.

For the second phase of the experiment, the bearings are placed vertical to the INSTRON System to provide the movement along shear direction.



Figure 4.17 Test set-up for the phase two

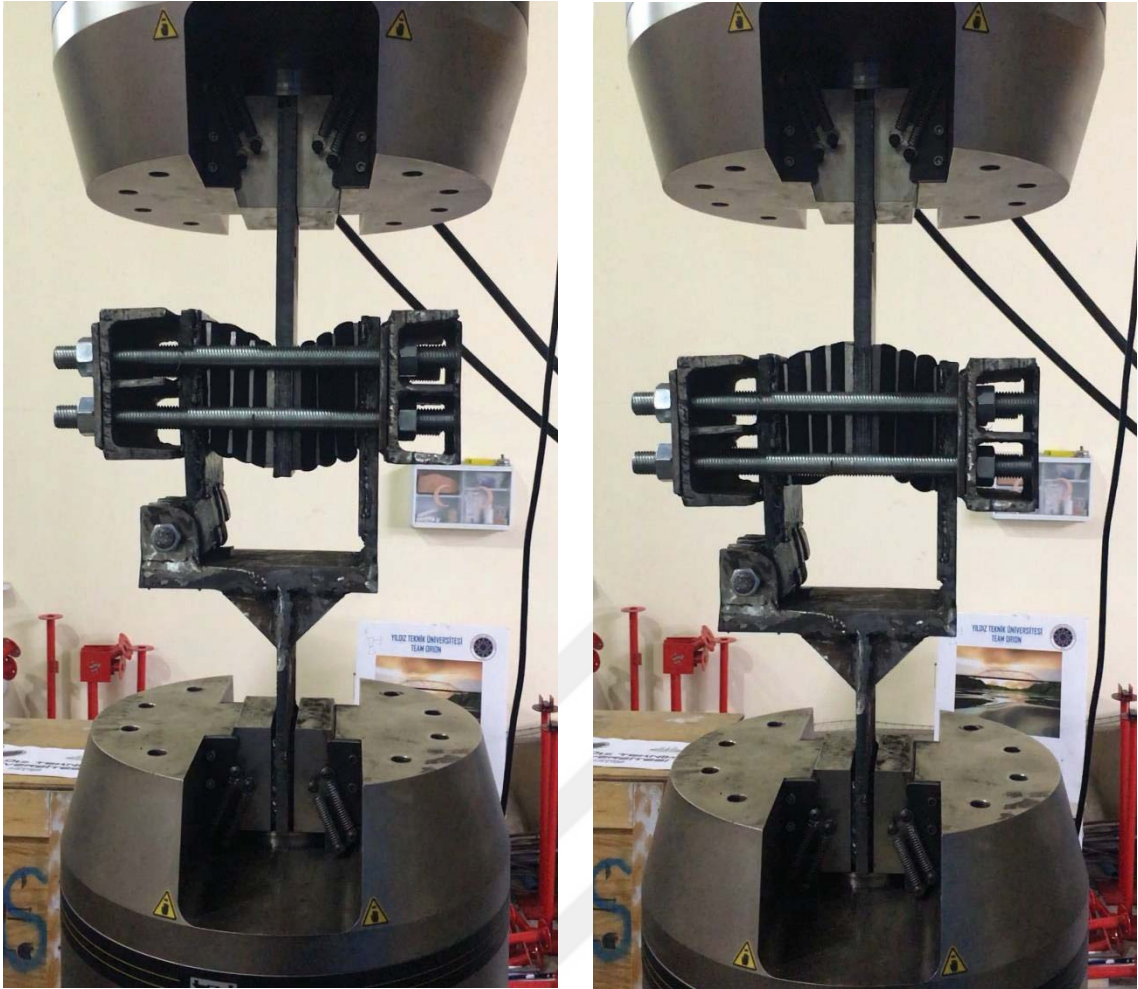


Figure 4.18 Movement along shear direction

Samples are forced to make movement equal to half of the thickness of a bearing and 10000 displacement-controlled loading and release cycles are carried out under 0.25 Hz frequency. These processes are repeated for 3 MPa, 4.5 MPa and 6 MPa compressive loads on different sample groups. The output data for the different compressive loadings are examined.

The first group of samples are axially forced under 3 MPa. Below, the force-displacement graph for the 100<sup>th</sup>, 1000<sup>th</sup>, 5000<sup>th</sup> and 10000<sup>th</sup> cycles can be seen.

100th Cycle

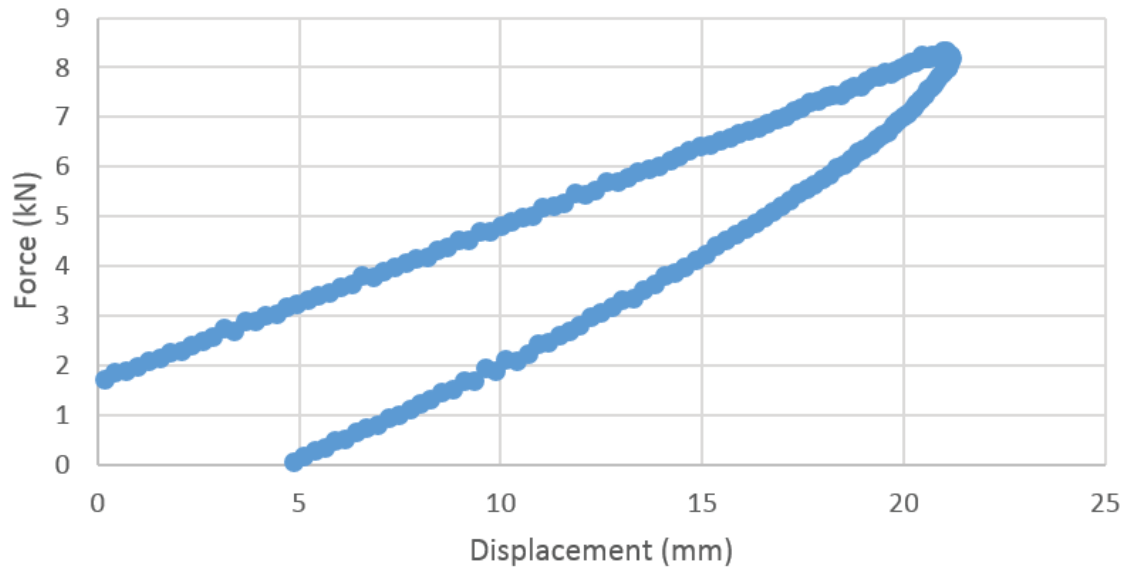


Figure 4.19 100<sup>th</sup> cycle under 3 MPa compression

1000th Cycle

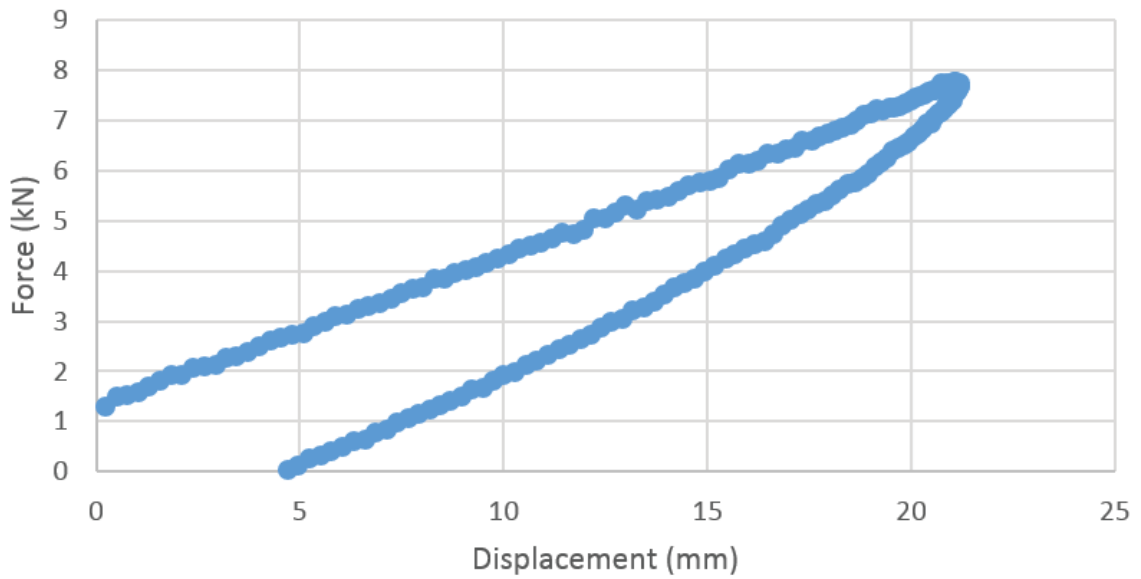


Figure 4.20 1000<sup>th</sup> cycle under 3 MPa compression

5000th Cycle

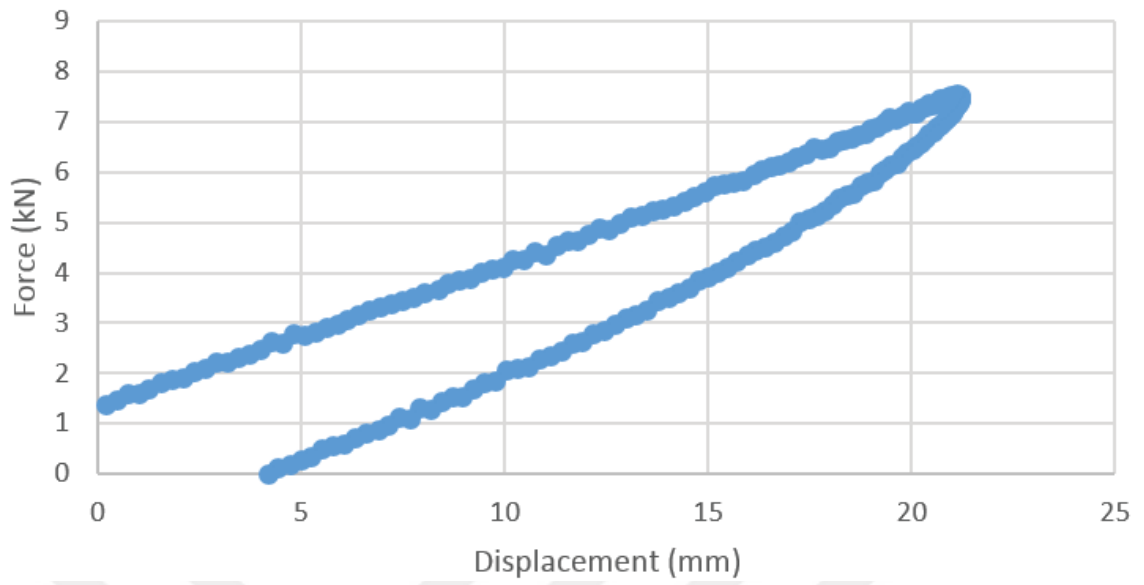


Figure 4.21 5000<sup>th</sup> cycle under 3 MPa compression

10000th Cycle

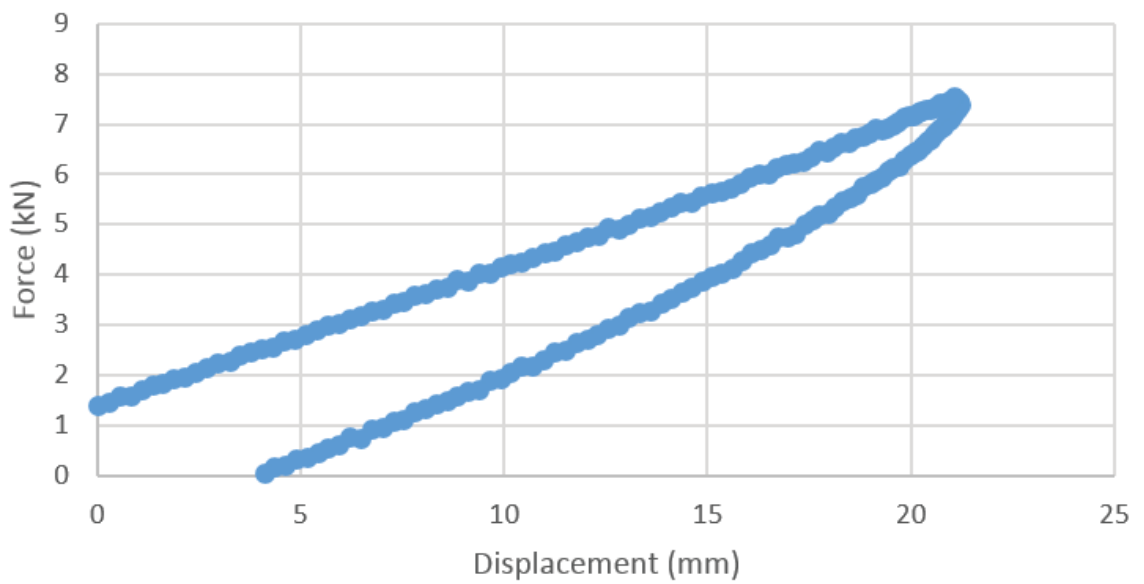


Figure 4.22 10000<sup>th</sup> cycle under 3 MPa compression

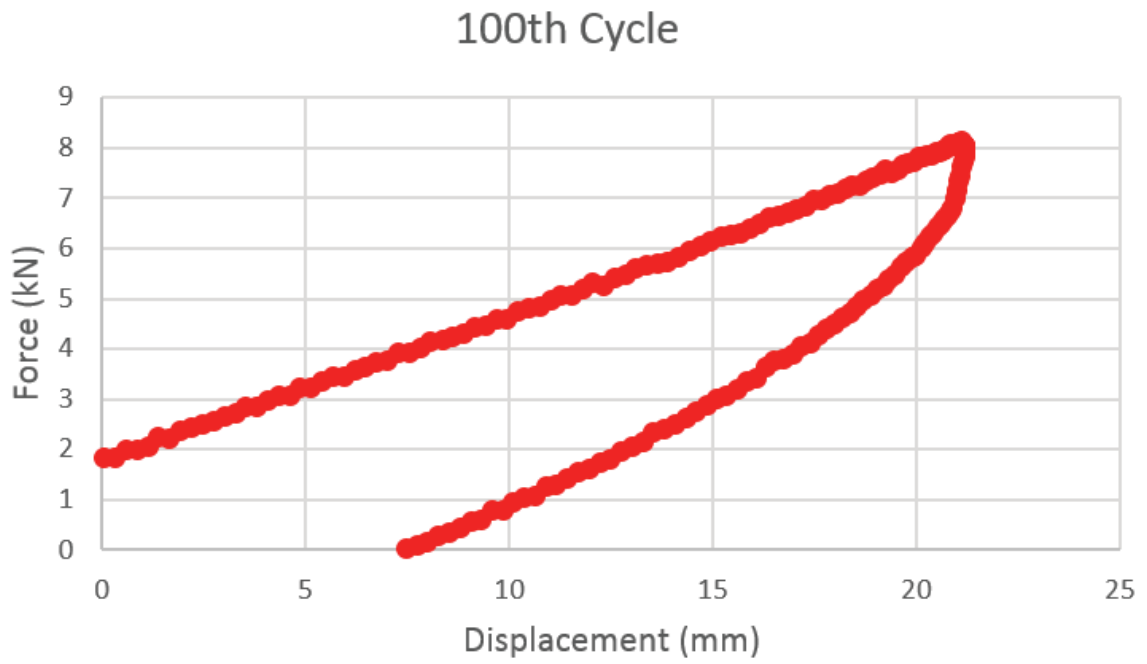


Figure 4.23 100<sup>th</sup> cycle under 4.5 MPa compression

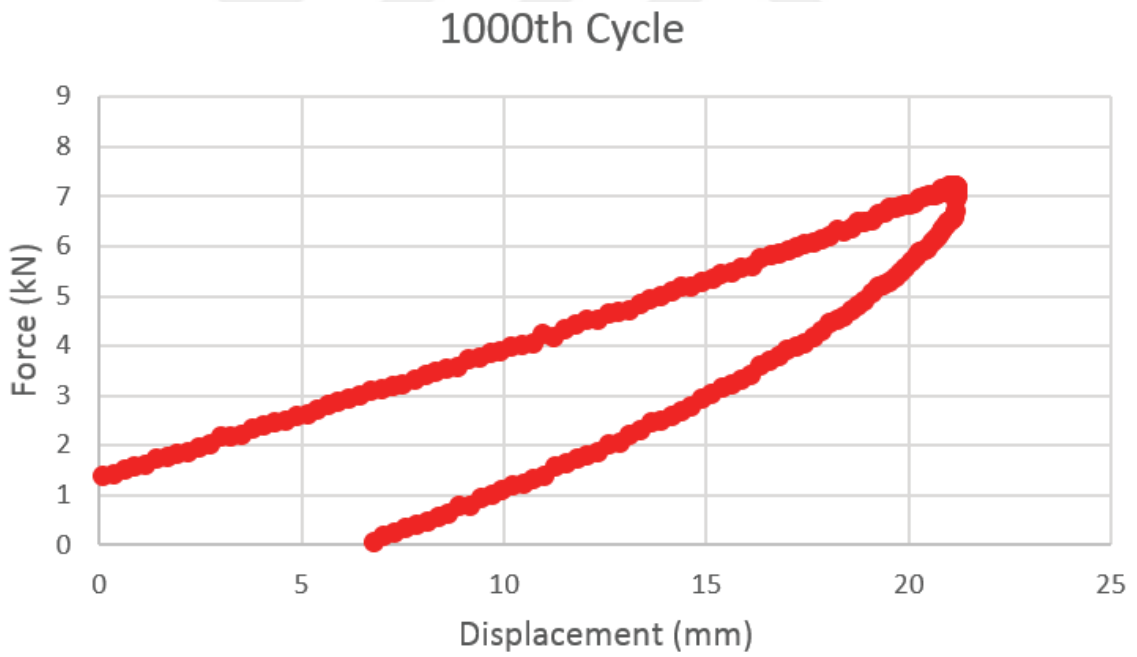


Figure 4.24 1000<sup>th</sup> cycle under 4.5 MPa compression



5000th Cycle

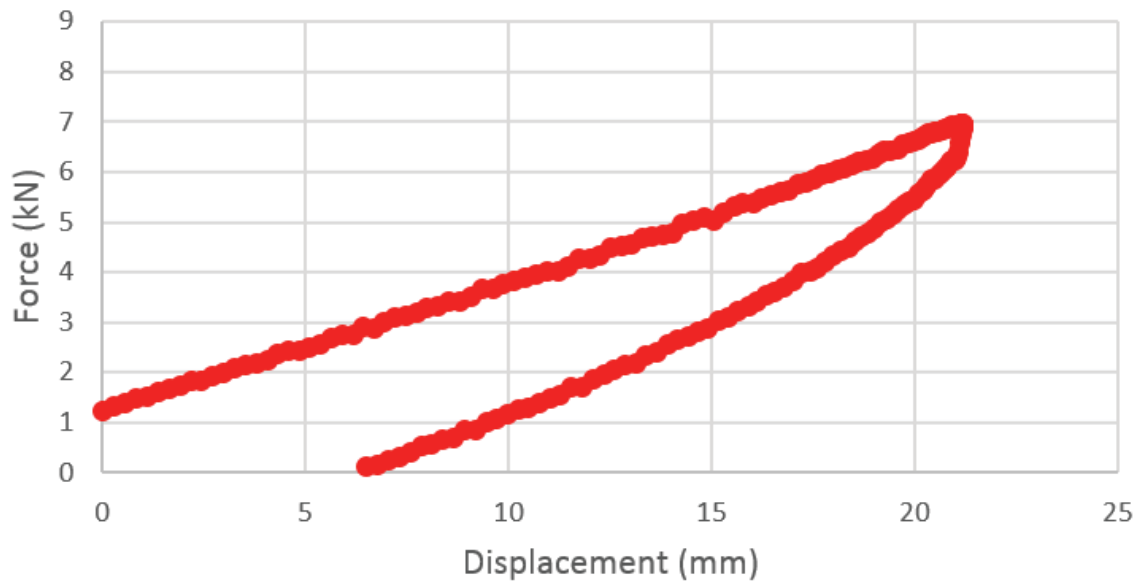


Figure 4.25 5000<sup>th</sup> cycle under 4.5 MPa compression

10000th Cycle

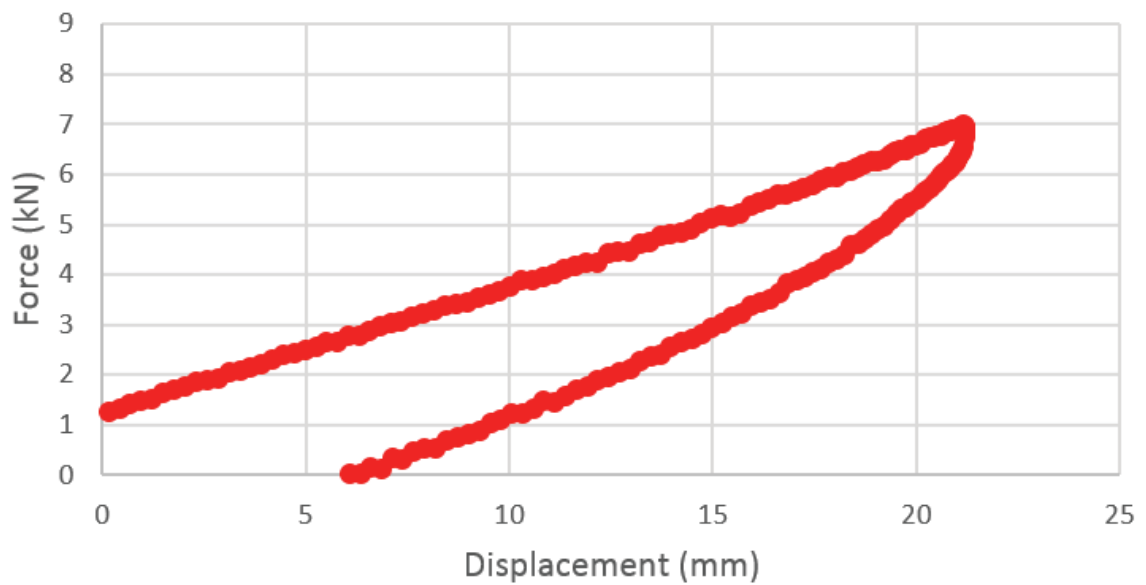


Figure 4.26 10000<sup>th</sup> cycle under 4.5 MPa compression

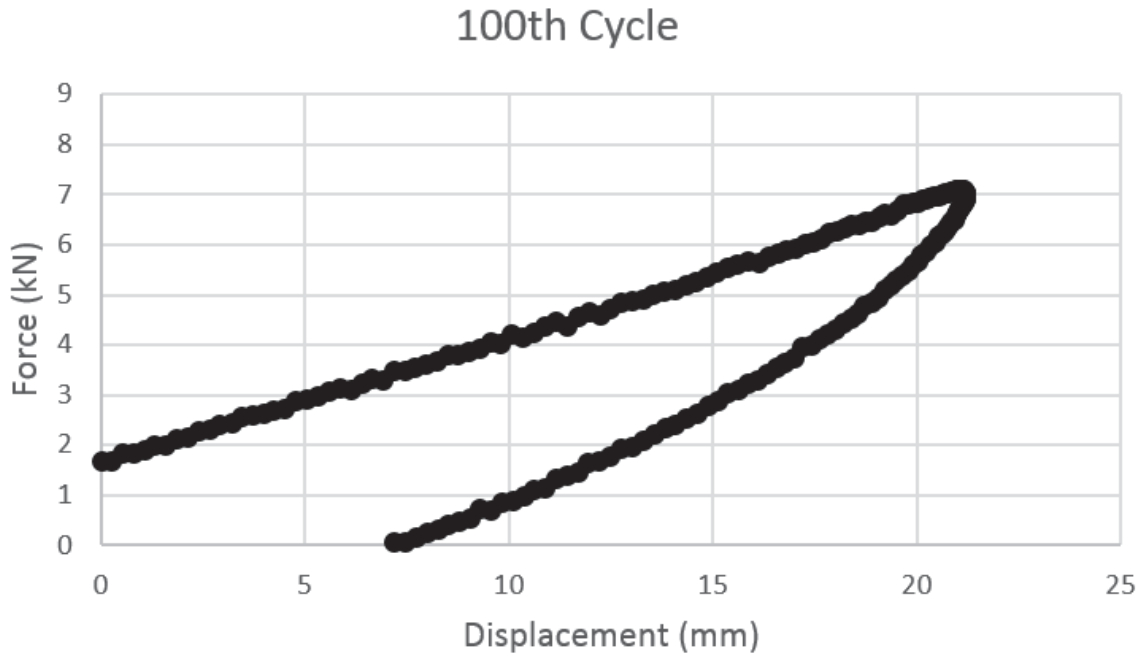


Figure 4.27 100<sup>th</sup> cycle under 6 MPa compression

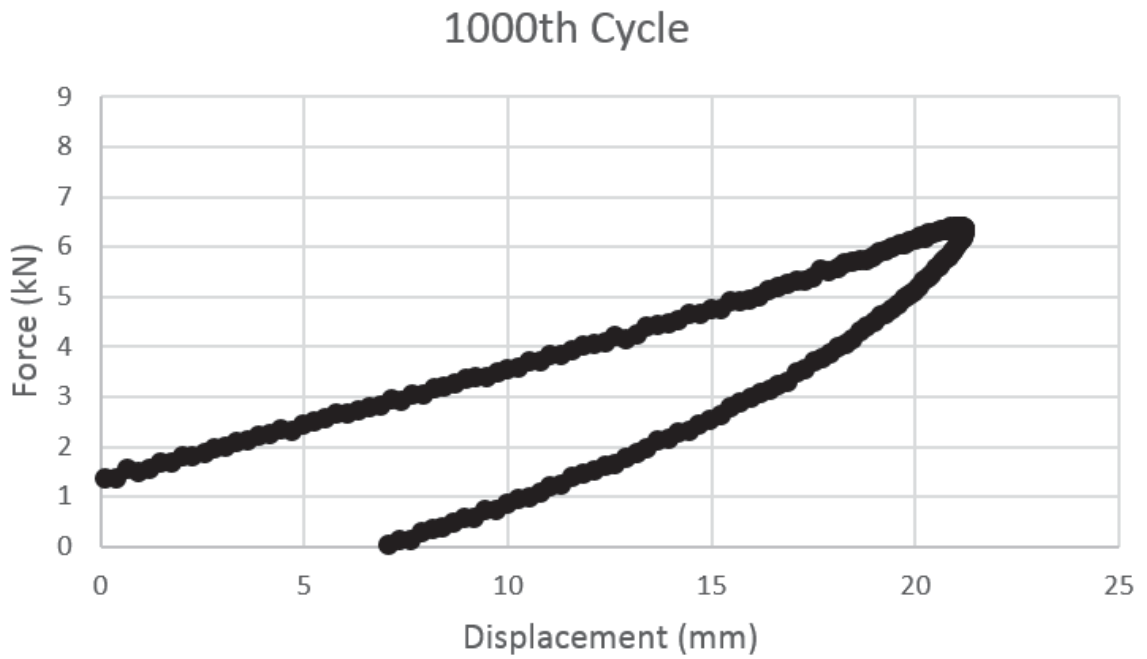


Figure 4.28 1000<sup>th</sup> cycle under 6 MPa compression

5000th Cycle

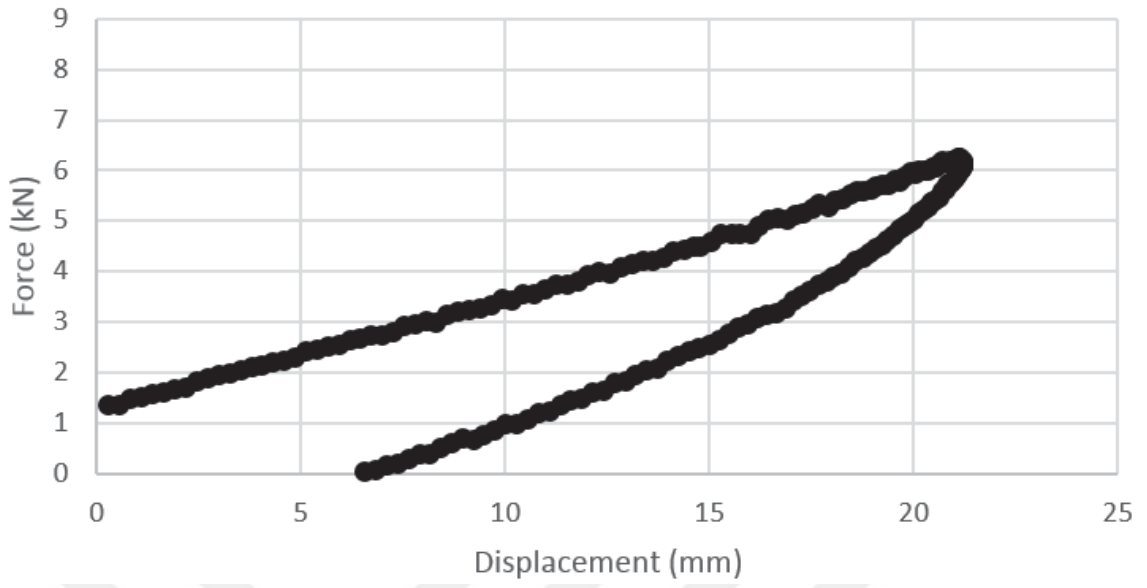


Figure 4.29 5000<sup>th</sup> cycle under 6 MPa compression

10000th Cycle

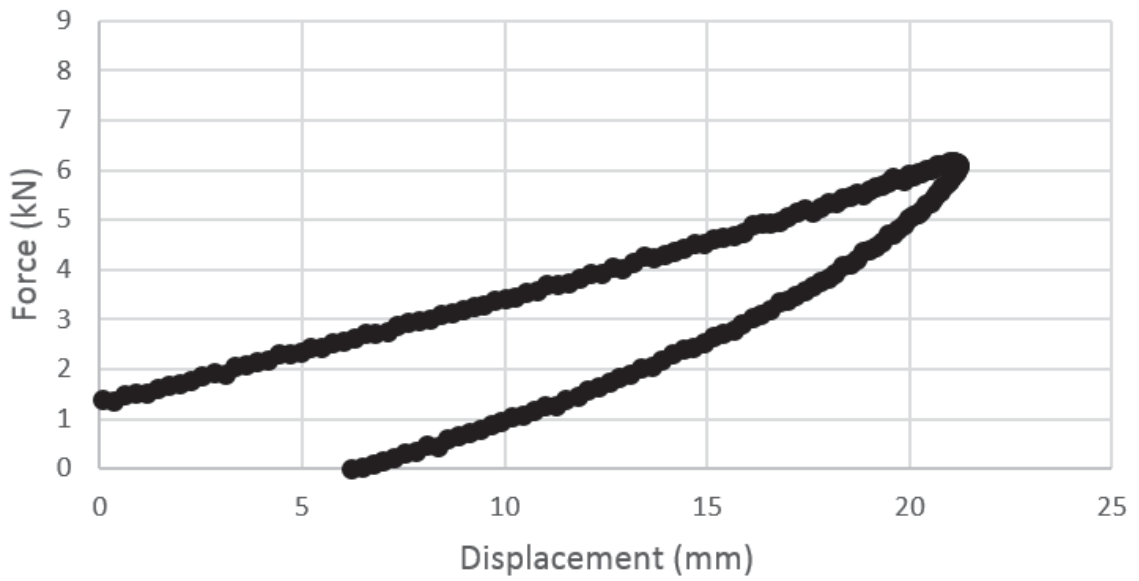


Figure 4.30 10000<sup>th</sup> cycle under 6 MPa compression

### COMPUTER-AIDED ANALYSIS

The experimental studies are generally executed under limited force and boundary conditions. Executing an experimental study for every possible condition may not be applicable because of the reasons beyond control such as financial problems, lack of time, not having appropriate devices etc. Therefore, the computer-aided analysis is a common way to get knowledge about material's behavior under desired conditions. Although the computer-aided analysis is more applicable compared to experimental studies, assigning the boundary conditions and material properties properly has vital importance. Assigning wrong conditions to the bearing model causes unrealistic result data, which may lead to poor interpretation and eventually unexpected performance problems in the structure. For this reason, computer aided analyses are required great attention.

## 5.1 Finite Element Model

One of the finite element analysis software ANSYS Workbench GUI v17 was used for the computational study. 3D view and dimensions of the bearing model is shown below.

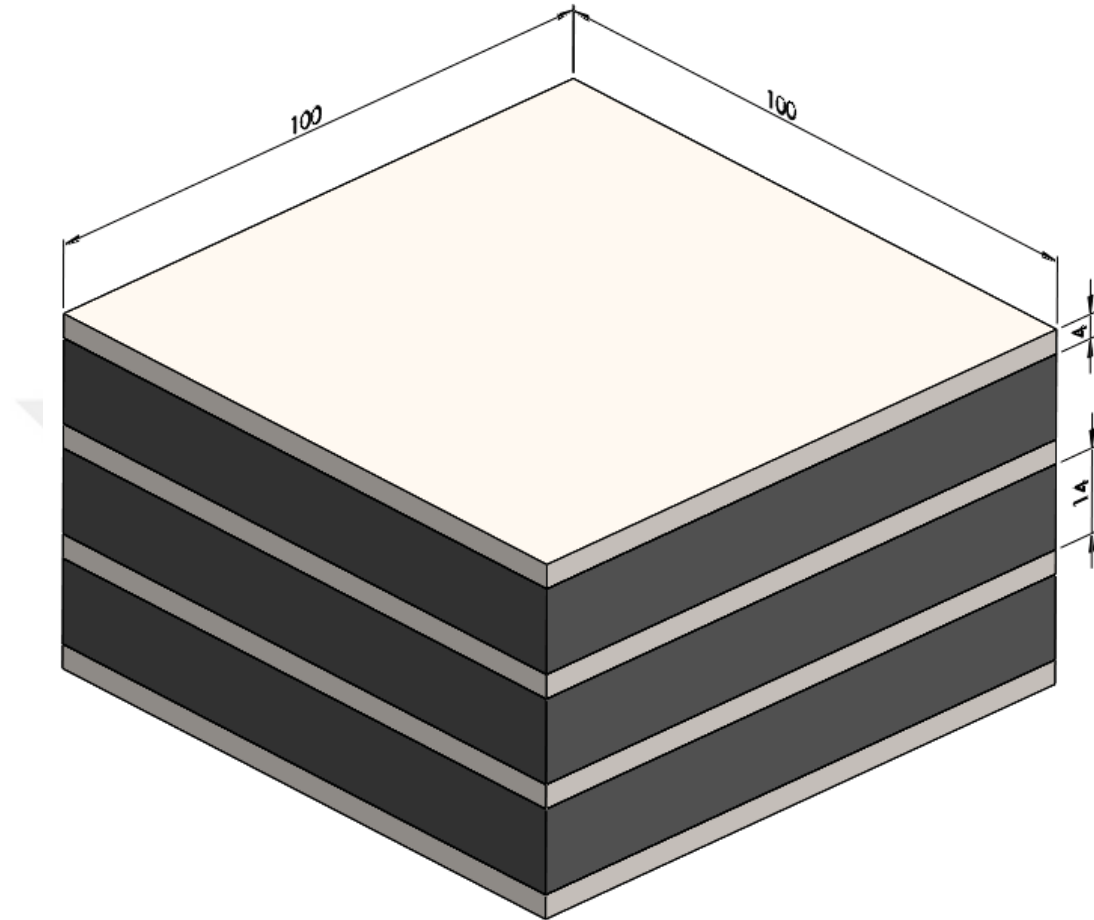


Figure 5.1 3D model and dimensions (mm) of the bearing sample model

In order to ensure that the bearing model and assigned boundary conditions are realistic, the result data of the computational analysis are compared to the results that obtained during the experimental studies. Hence, various computational analyses are executed. These analyses have the same conditions (compression load and forced lateral movement) with experimental studies. Thus, once the relative error between the experimental and computational studies are low enough, it means that the finite element model is converged.

## 5.2 Mesh Elements and Overcoming the Convergence Failure

Meshing has significant factor for a successful finite element analysis. Using more mesh elements generally provide the results to be more accurate unless any singularity problem occurs. Singularities in finite element analysis can be described as unrealistic stress concentration in a certain zone/zones which occur as a result of geometrical shape, poor boundary conditions, point loads etc. A special treatment is required to overcome this problem.

One of the key points about meshing is considering the computational time it causes. Fine mesh elements mean higher number of nodes and degree of freedom which eventually lead to higher computational time. Besides, the selected mesh element type has significant effect on computational requirements. ANSYS provides large variety of element types for various kind of analysis. There are four shape of mesh elements which are point, line, area and volume. Shape of these elements are determined according to the geometrical shape of the model and the type of the analysis.

In this study, volume elements are automatically generated since the type of analysis is three dimensional. The types of volume elements differ from each other by their purpose of usage (structural, thermal, electromagnetic etc.), shape, number of nodes and number of degrees of freedom at each node.

For instance, SOLID70 type of elements are used for 3D, steady-state or transient thermal analysis and have 8 nodes with a single degree of freedom, temperature, at each node.

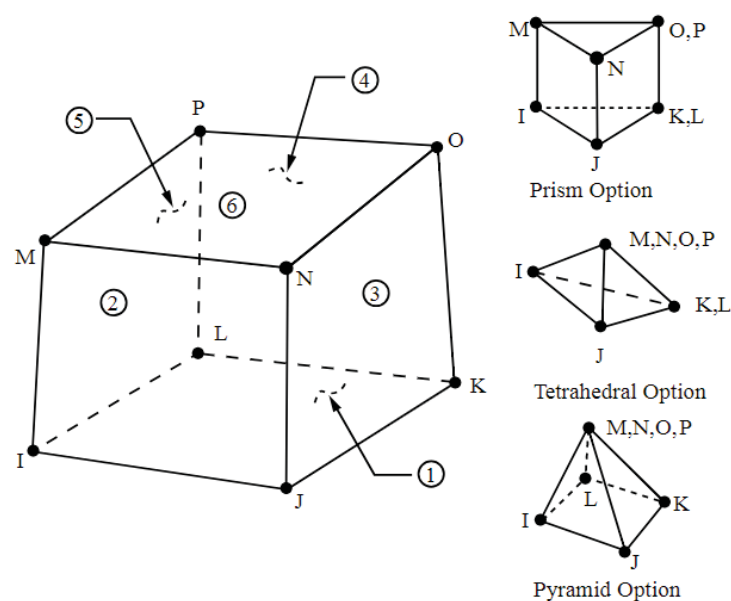


Figure 5.2 Illustration of the SOLID70 type of mesh element

As another example for thermal elements, SOLID90 is recommended for the same analysis type with SOLID70. The difference between these two types comes from the additional nodes between the main nodes. These nodes provide high accuracy with less elements.

There are three common structural solid elements named SOLID185, SOLID186 and SOLID187. These elements support large displacement and large strain capabilities of nearly or fully incompressible hyperelastic materials and each node has three degrees of freedom which are translations in the nodal x, y and z directions.

SOLID187 has tetrahedral geometrical shape and mid-side nodes. If the model is wanted to be meshed with tetrahedral elements, ANSYS Workbench uses these elements as default.

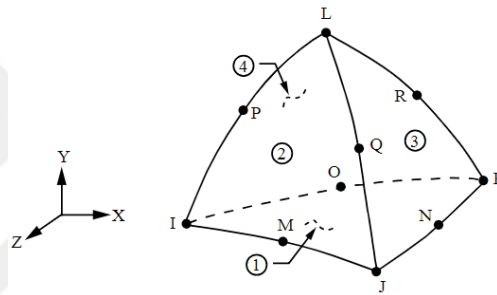


Figure 5.3 Illustration of the SOLID187 type of mesh element

SOLID185 elements have eight nodes but no mid-side nodes. Similar to other types of elements, it has prism, tetrahedral and pyramid options but the tetrahedral and pyramid options are not recommended since these options have high aspect ratio without additional nodes.

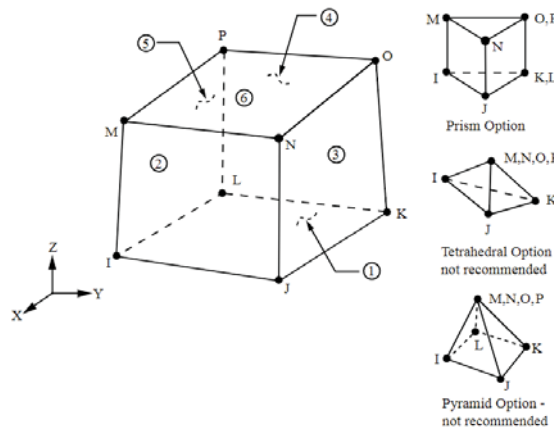


Figure 5.4 Illustration of the SOLID185 type of mesh element

SOLID186 is a higher-order version of SOLID185. It has 20 nodes in total including the mid-side nodes.

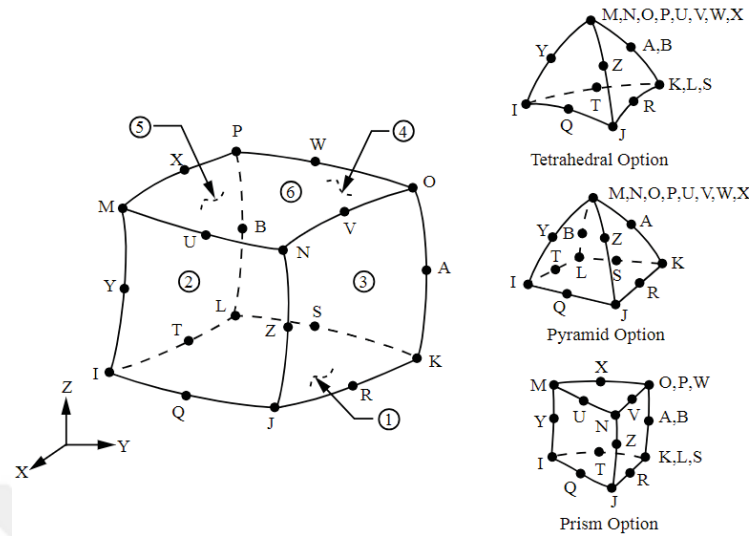


Figure 5.5 Illustration of the SOLID186 type of mesh element

Having additional nodes provides more accurate results with less elements. Therefore, SOLID186 type elements are chosen for the mesh process.

As the first precaution for a possible convergence failure, the analysis divided into more steps. Increasing the number of load steps to decrease the sudden increment of the load generally solves these kinds of errors. Therefore, the analysis is divided up into 35 steps. Each step consists of 4 sub-steps unless any bisection occurs. After the compression loading is completed at the end of the first 14 steps, the horizontal movement is applied in the last 21 steps.

During the first meshing studies, the thickness of rubber blocks were divided into four layers. However, the convergence failure occurred during the analysis under high compression loads. The Displacement Convergence graph of an unsuccessful analysis with multi-steps is demonstrated below.



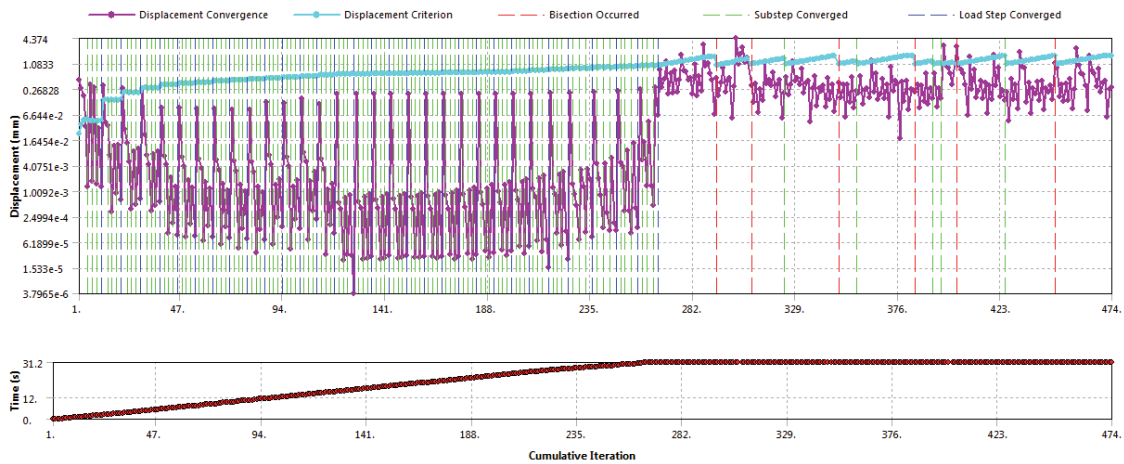


Figure 5.6 Displacement convergence graph

The graph shows that the equilibrium iterations could not be solved during the 31<sup>st</sup> and 32<sup>nd</sup> seconds, which means the compression loads are applied successfully but the convergence failure started to occur during the horizontal movement. Bisections that have occurred after a certain number of steps can be seen as red lines in the graph.

Bisection is a feature to overcome the convergence failure by cutting the time step size in half and restarting the iteration from the last converged sub-step until the convergence is achieved. If the convergence could not be achieved until the specified minimum time step size is reached, the analysis stops. To see the reason of this convergence failure, the Solver Output data should be examined. The error message in Solver Output is shown below.

```

*** ERROR ***                               CP = 4993.811  TIME= 02:49:38
Element 4096 (type = 6, SOLID186) (and maybe other elements) has become
highly distorted.

```

Figure 5.7 Error message emphasizing element distortions

High element distortion is the most common problem in a finite element analysis with large strains. By using the Named Selection tool, it is observed that the distorted elements are in the rubber layer which is the most unfavorable zones of the bearing because of the bulging effect and shear movement with large strain levels. Since the number of steps is relatively adequate, quality of the mesh elements is improved to overcome this convergence failure.

The goal of the mesh refinement is providing the high accuracy with the lowest computational cost. Computational cost means not only the computational time, but also the hardware limits. For instance, it is likely the analysis to be stopped with a warning

message that indicates the lack of physical memory (RAM) and CPU time if the hardware capacity was not taken into account during the mesh refinement process.

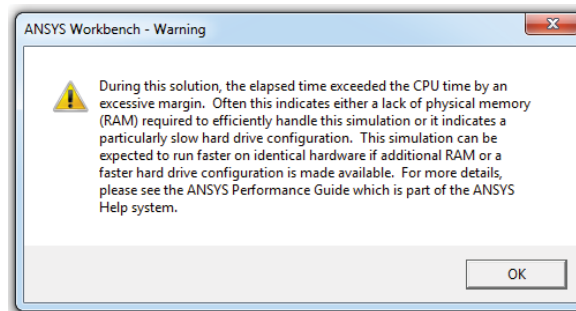


Figure 5.8 Warning message emphasizing high computational cost

After some mesh refinement studies and test analysis, it's determined to divide the rubber layers into 6 layers with mesh elements considering the computational time and convergence criteria. Final mesh condition is illustrated below:

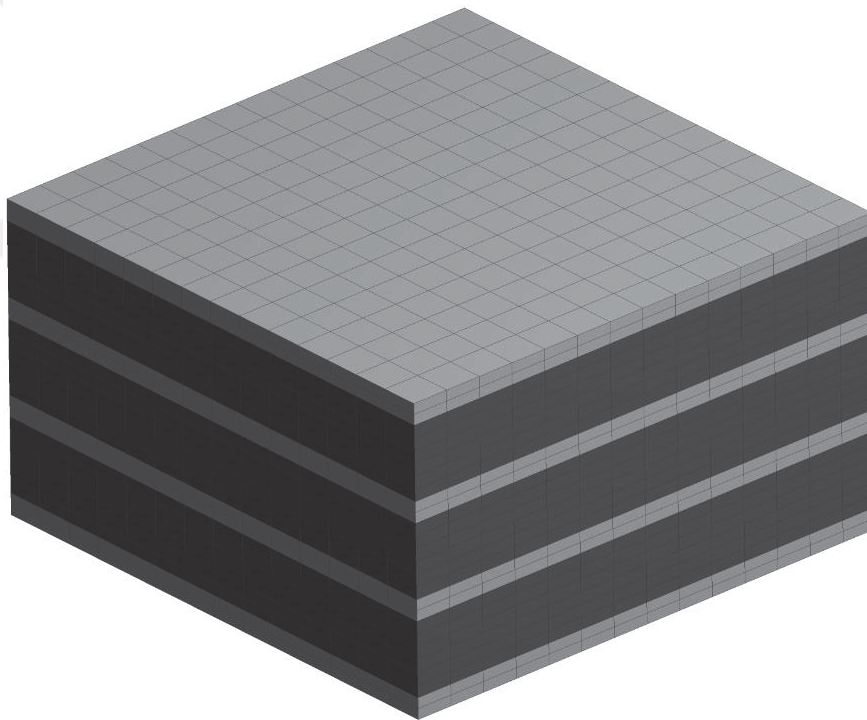


Figure 5.9 Ultimate mesh condition of the finite element model

### 5.3 Hyperelastic Material Models

Theoretical background about hyperelastic material models is given before proceeding to material definition. It should be noted that hyperelastic materials are generally treated as incompressible (poisson ratio  $\nu \approx 0.5$ ), therefore the rubber layers of the elastomeric bearing are assumed as fully incompressible in this study.

The main difference between hyperelastic material models generally comes from the derivation of strain energy density function,  $W$ . Since the hyperelastic materials' behavior are more complex compared to elastic linear materials behaviors, various models are developed over time according to experimental studies and observations. Some of the commonly used hyperelastic material models Mooney-Rivlin, Neo-Hookean and Ogden models are explained briefly.

*Mooney-Rivlin* is a hyperelastic material model where the strain energy function is created with two invariants of the left Cauchy-Green deformation tensor. It was proposed by Melvin Mooney in 1940 and improved by Ronald Rivlin in 1948. The model has relatively low computational cost and high accuracy up to 200% strain level.

There are four variations of Mooney-Rivlin model according to the number of material constants used in the function. Formulations of the strain energy function for this model are as follows:

2-Parameters

$$W_{(2)} = C_{10}(\bar{I}_1 - 3) + C_{01}(\bar{I}_2 - 3) + \frac{1}{d}(J - 1)^2 \quad (5.1)$$

3-Parameters

$$W_{(3)} = C_{10}(\bar{I}_1 - 3) + C_{01}(\bar{I}_2 - 3) + C_{11}(\bar{I}_1 - 3)(\bar{I}_2 - 3) + \frac{1}{d}(J - 1)^2 \quad (5.2)$$

5-Parameters

$$W_{(5)} = C_{10}(\bar{I}_1 - 3) + C_{01}(\bar{I}_2 - 3) + C_{11}(\bar{I}_1 - 3)(\bar{I}_2 - 3) + C_{20}(\bar{I}_1 - 3)^2 + C_{02}(\bar{I}_2 - 3)^2 + \frac{1}{d}(J - 1)^2 \quad (5.3)$$

9-Parameters

$$W_{(9)} = C_{10}(\bar{I}_1 - 3) + C_{01}(\bar{I}_2 - 3) + C_{11}(\bar{I}_1 - 3)(\bar{I}_2 - 3) + C_{20}(\bar{I}_1 - 3)^2 + C_{02}(\bar{I}_2 - 3)^2 + C_{30}(\bar{I}_1 - 3)^3 + C_{21}(\bar{I}_1 - 3)^2(\bar{I}_2 - 3) + C_{12}(\bar{I}_1 - 3)(\bar{I}_2 - 3)^2 + C_{03}(\bar{I}_2 - 3)^3 + \frac{1}{d}(J - 1)^2 \quad (5.4)$$

Where  $\bar{I}_1$  and  $\bar{I}_2$  are the first and second deviatoric strain invariants,  $C_{ij}$  is the material constant,  $J$  is the ratio of the deformed volume over the undeformed volume and  $d$  is the material incompressibility parameter which can be estimated from volumetric test data.

Material constants can be used for the determination of initial shear modulus. Regardless of the number of parameter used, the initial shear modulus  $\mu_0$  is always found as:

$$\mu_0 = 2(C_{10} + C_{01}) \quad (5.5)$$

The first and second deviatoric strain invariants can be described as:

$$\bar{I}_1 = \bar{\lambda}_1^2 + \bar{\lambda}_2^2 + \bar{\lambda}_3^2 \quad (5.6)$$

$$\bar{I}_2 = \bar{\lambda}_1^{(-2)} + \bar{\lambda}_2^{(-2)} + \bar{\lambda}_3^{(-2)} \quad (5.7)$$

Deviatoric stretch value  $\bar{\lambda}_i$  is obtained from the equation below:

$$\bar{\lambda}_i = J^{-1/3} \lambda_i \quad (5.8)$$

Where  $\lambda_i$  values are the principal stretches.

The determination of the suitable number of parameters to be used should be done depending on the inflection points on the stress-strain graph.

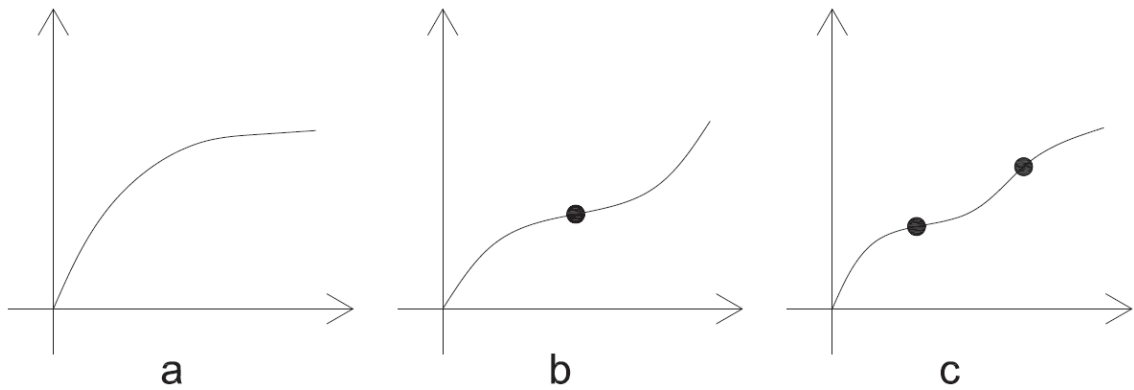


Figure 5.10 Stress-Strain graphs with none (a), one (b) and two (c) inflection points

If the stress-strain graph type is single curvature (a), the type of Mooney-Rivlin model can be chosen as 2 or 3 parameters. If the graph has one inflection point (b), 3 or 5 parameters version of the hyperelastic model can be used. In the case of having stress-strain graph with two inflection points (c), 5 or 9 parameters versions should be chosen.

*Neo-Hookean* material model was proposed by Ronald Rivlin and can be described as a special form of 2-Parameters Mooney-Rivlin Model which  $C_{01}$  is equal to 0 and. Thus, the strain energy density function for an incompressible material is as follows:

$$W = C_{10}(\bar{I}_1 - 3) + \frac{1}{d}(J - 1)^2 \quad (5.9)$$

The initial shear modulus is found as:

$$\mu_0 = 2C_{10} \quad (5.10)$$

Neo-Hookean is the simplest hyperelastic material model and recommended to be used when the material data is insufficient. It has the fastest computational speed and good approximation at relatively small strains but leads to inaccurate results at large strains.

*Ogden* material model differs from the other two models by the derivation of energy density function. The model is based on principal stretches unlike the Mooney-Rivlin and Neo-Hookean models which are based on strain invariants. Energy density function for the Ogden model is:

$$W = \sum_{i=1}^N \frac{\mu_i}{\alpha_i} (\lambda_1^{\alpha_i} + \lambda_2^{\alpha_i} + \lambda_3^{\alpha_i} + \lambda_4^{\alpha_i} - 3) + \sum_{k=1}^N \frac{1}{D} (J - 1)^{2k} \quad (5.11)$$

While  $\alpha_i$  and  $\mu_i$  values are determined with experimental data,  $N$  value emphasizes the order of the model. After the order of the model is determined, the initial shear modulus is found as:

$$\mu_0 = \sum_{i=1}^N \mu_i \quad (5.12)$$

It should be noted that the Ogden model can be converted to Neo-Hookean by defining the values as  $N=1$ ,  $\alpha_1=2$ . For the  $N=2$ ,  $\alpha_1=2$  and  $\alpha_2=-2$  values, Mooney-Rivlin model can be obtained as well.

Ogden material model has the highest computational cost among other mentioned models but in return, the behavior of rubber-like materials can be simulated with high accuracy at large strains (up to 700%) especially with the 3rd Order Ogden Model ( $N=3$ ).

## 5.4 Hyperelastic Material Definition in ANSYS Workbench

Determination of the hyperelastic material constants using ANSYS Workbench is quite simplified with Engineering Data module. Below, the provided hyperelastic material models are shown.

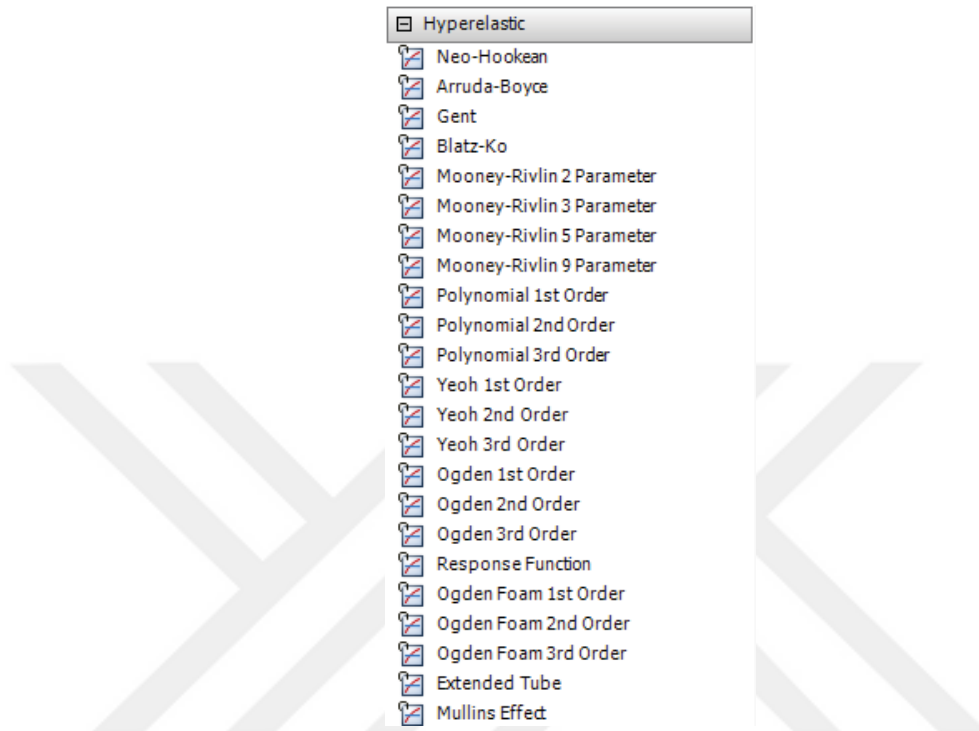


Figure 5.11 Hyperelastic material models in ANSYS

As can be seen, ANSYS provides large variety of hyperelastic material models. In this study, Mooney-Rivlin hyperelastic material model with 5 parameters was used considering the accuracy and computational cost of the model. After selecting the Mooney-Rivlin 5 Parameter module, software fills the required constants with yellow color.

Properties of Outline Row 5: Mooney-Rivlin 5 Parameter				
	A	B	C	D E
1	Property	Value	Unit	
2	Mooney-Rivlin 5 Parameter			
3	Material Constant C10		Pa	
4	Material Constant C01		Pa	
5	Material Constant C20		Pa	
6	Material Constant C11		Pa	
7	Material Constant C02		Pa	
8	Incompressibility Parameter D1		Pa <sup>-1</sup>	

Figure 5.12 Required material constants

Material constants are not independent of each other and affect the general behavior of the rubber together, so it is essential to input correct values. If the constants are not known, experimental data can be evaluated with the Curve Fitting feature.

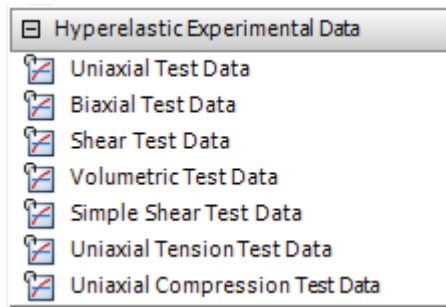


Figure 5.13 Hyperelastic experimental data modules

Curve fitting is a tool for the determination of hyperelastic material model constants by given experimental data. The essential inputs for the usage of this feature are Uniaxial, Biaxial and Shear test data. Since the uniaxial and biaxial experiments were not executed in this study, the result data for another rubber material are used in the first analysis. Later, the accuracy problem caused by this situation is tried to be prevented by making some modifications based on the shear test data obtained from the previous chapter.

Properties of Outline Row 5: Mooney-Rivlin 5 Parameter				
	A	B	C	D E
1	Property	Value	Unit	
2	Uniaxial Test Data	Tabular		
3	Biaxial Test Data	Tabular		
5	Shear Test Data	Tabular		
7	Mooney-Rivlin 5 Parameter			
8	Material Constant C10		Pa	
9	Material Constant C01		Pa	
10	Material Constant C20		Pa	
11	Material Constant C11		Pa	
12	Material Constant C02		Pa	
13	Incompressibility Parameter D1		Pa <sup>-1</sup>	
14	Curve Fitting	Fit Type: Mooney-Rivlin 5 Parameter		
15	Error Norm for Fit	Normalized Error		
16	Uniaxial Test Data	Tabular		
17	Biaxial Test Data	Tabular		
18	Shear Test Data	Tabular		

Figure 5.14 Required test data for the determination of material constants

### 5.5 Executing Finite Element Analyses

In this chapter, the bearing model is forced to make horizontal movements with & without continuous compression loads same as the experiments and the results are compared to experimental data.

Since the material behavior of the rubber is nonlinear, the comparisons are needed to be done by considering more than one step in order to observe the change at relative error over displacement. In this study, the simulation results indicating reaction forces occurred during 7 mm (17% strain), 14 mm (33% strain) and 21 mm (50% strain) lateral movement are shown, in order to compare with experimental results in the following chapter.

Uniaxial, biaxial and shear test data for different rubber material is used for the first analyses. As a result, the lateral load that force the sample to make horizontal movement was observed quite high compared to the experimental data. This indicates that the experimented rubber material had high stiffness compared to the rubber used in this study. After, the accuracy problem tried to be solved by using the shear data obtained from the previous chapter and modifying the uniaxial and biaxial test data based on the difference at shear behavior of these different rubber materials.

The modified stress-strain graph for uniaxial, biaxial and shear data is illustrated below.

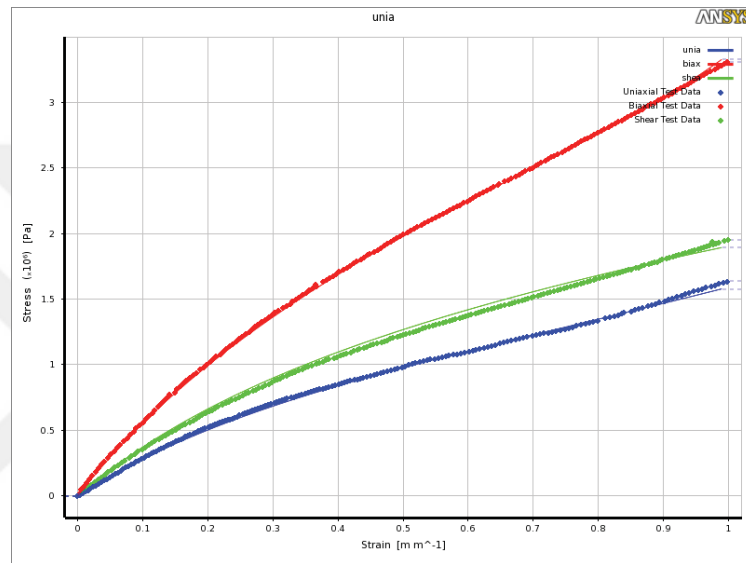


Figure 5.15 Modified stress-strain graphs

The material constants determined by ANSYS Engineering Data Module are as follows:

C10: 0.309 MPa, C01: 0.226 MPa, C20:0.031 MPa,

C11: -0.045 MPa, C02: 0.008 MPa, D1: 0 Pa<sup>-1</sup> (Fully incompressible)

### 5.5.1.1 Without Compression Load

After the definition of material constants, the bearing model is analyzed without any compression load as a start. The analysis is divided up into 21 steps (1 mm at each step) to prevent convergence failure that may occur at large strain levels. Deformed shape and reaction forces along horizontal direction are shown below:



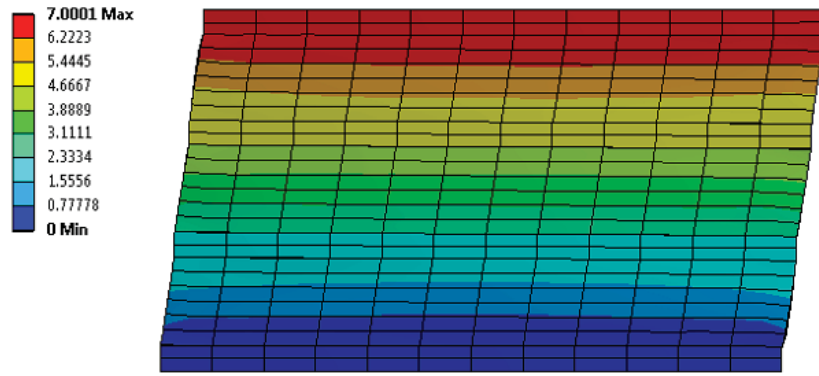


Figure 5.16 Deformed shape at 17% strain (7 mm)

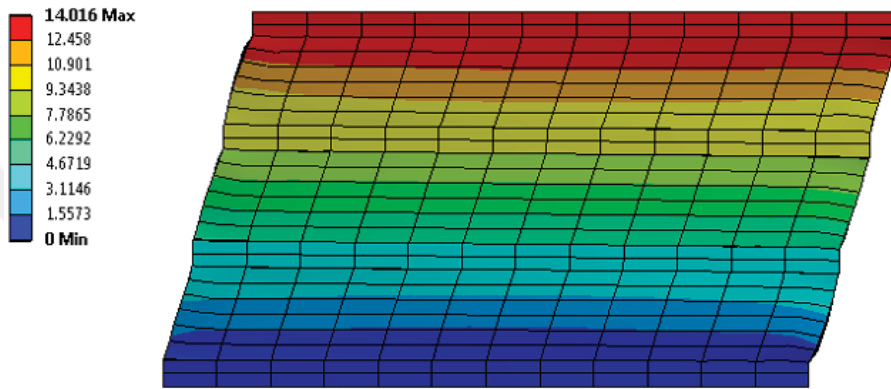


Figure 5.17 Deformed shape at 33% strain (14 mm)

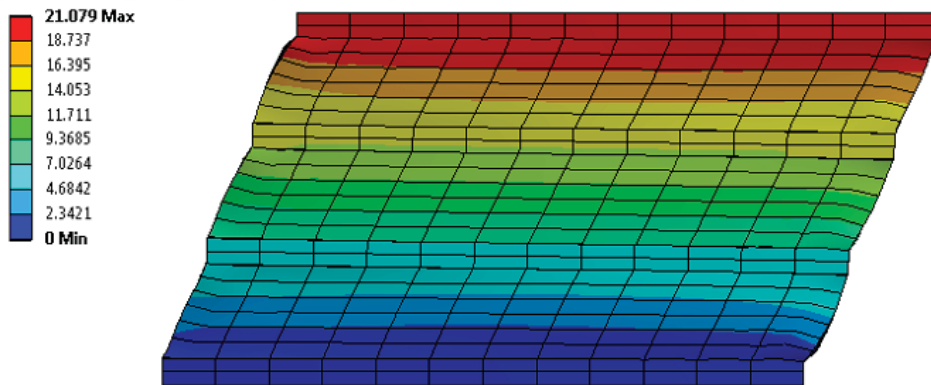


Figure 5.18 Deformed shape at 50% strain (21 mm)

Table 5.1 Reaction forces at specified lateral strain level (without compression load)

Lateral Displacement (mm)	Reaction Force (kN)
7 (17% Strain)	1.49
14 (33% Strain)	3.11
21 (50% Strain)	4.75

### 5.5.1.2 Under Compression Load

In this chapter, the lateral behavior of the finite element model is examined under compression loads. The bearing model is forced to make 50% strain under 3, 4.5 and 6 MPa compression loads as experimented in related chapter.

As mentioned before, the analyses have been divided up into 35 steps. The first 14 steps are for the application of compression load, while the last 21 steps are for the forced horizontal movement. The result data at the end of 14<sup>th</sup>, 21<sup>st</sup> (lateral 7 mm), 28<sup>th</sup> (lateral 14 mm) and 35<sup>th</sup> (lateral 21 mm) steps are shown at each chapter.

#### 5.5.1.2.1 Under 3 MPa Compression

Deformed shape of the finite element model after the specified step.

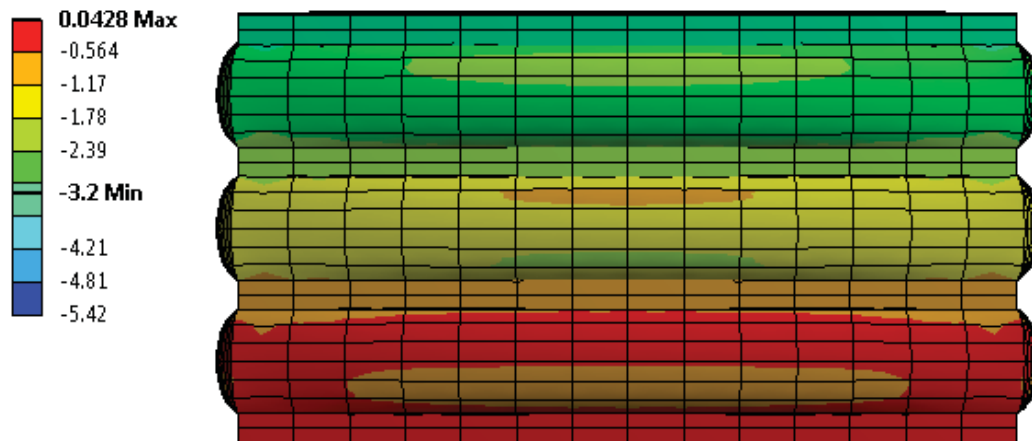


Figure 5.19 Axial deformation under 3 MPa compression load (14<sup>th</sup> Step)

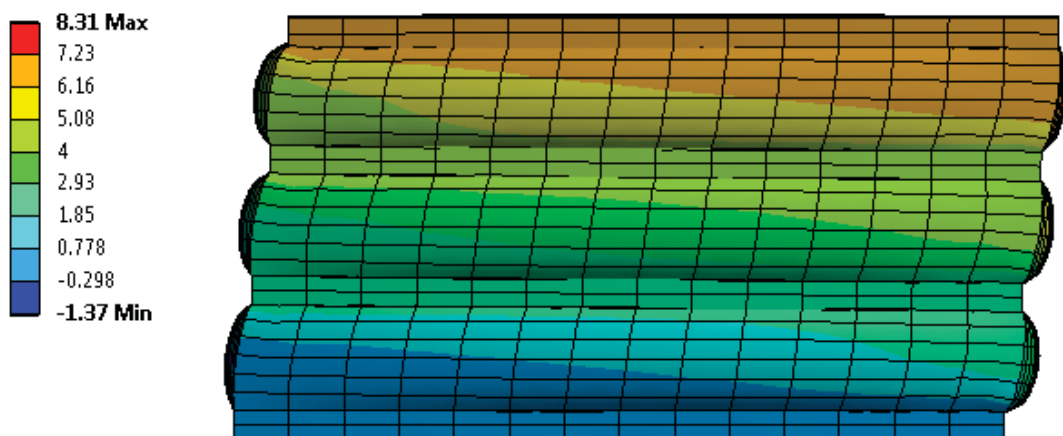


Figure 5.20 Lateral deformation at 17% strain (21<sup>st</sup> Step) (Under 3 MPa compression)

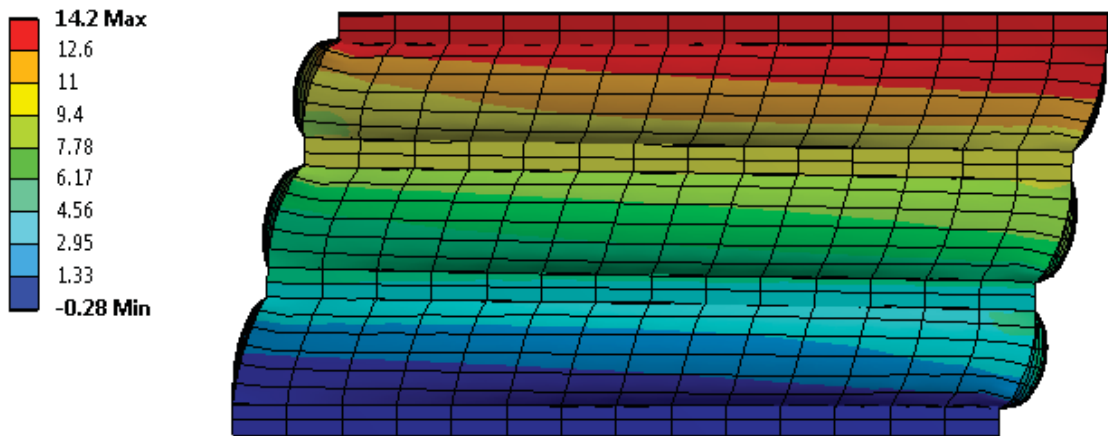


Figure 5.21 Lateral deformation at 33% strain (28<sup>st</sup> Step) (Under 3 MPa compression)

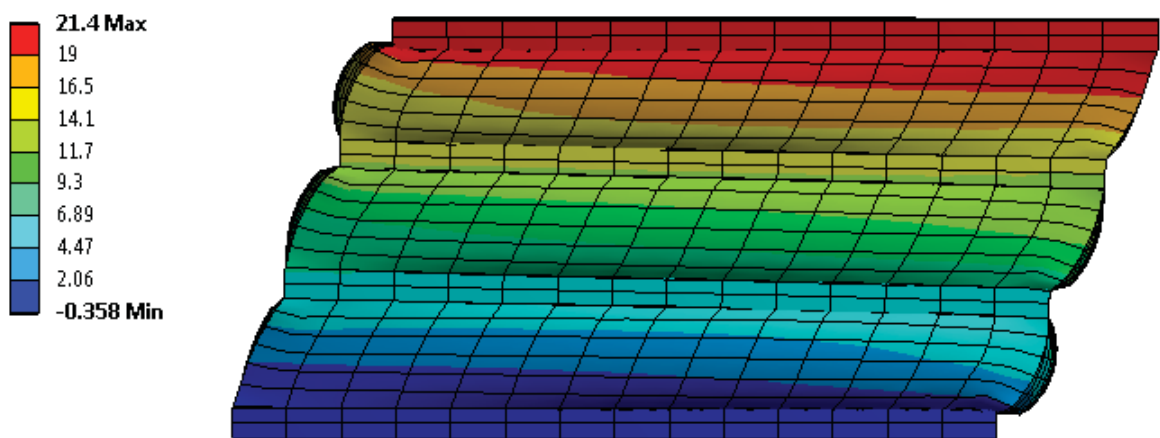


Figure 5.22 Lateral deformation at 50% strain (35<sup>th</sup> Step) (Under 3 MPa compression)

Table 5.2 Reaction forces at specified lateral strain level (3 MPa compression load)

Lateral Displacement (mm)	Reaction Force (kN)
7 (17% Strain)	1.35
14 (33% Strain)	2.66
21 (50% Strain)	3.98

### 5.5.1.2.2 Under 4.5 MPa Compression

Deformed shape of the finite element model after the specified step.

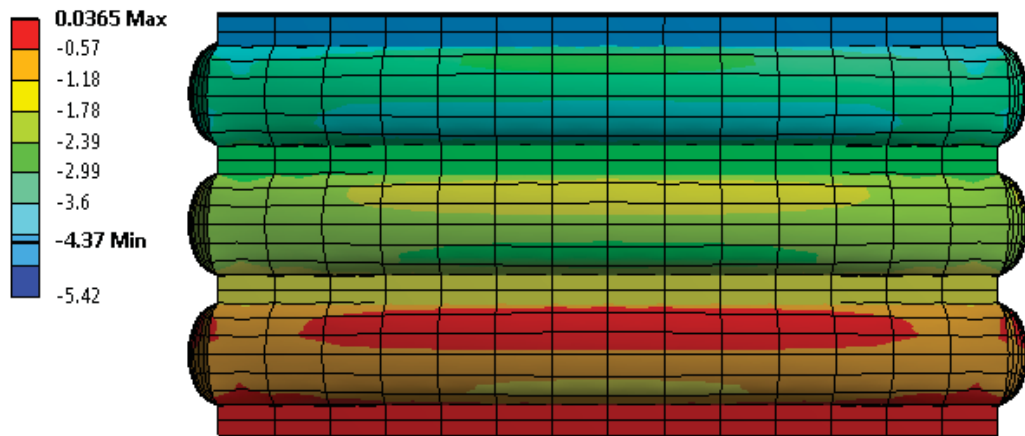


Figure 5.23 Axial deformation under 4.5 MPa compression load (14<sup>th</sup> Step)

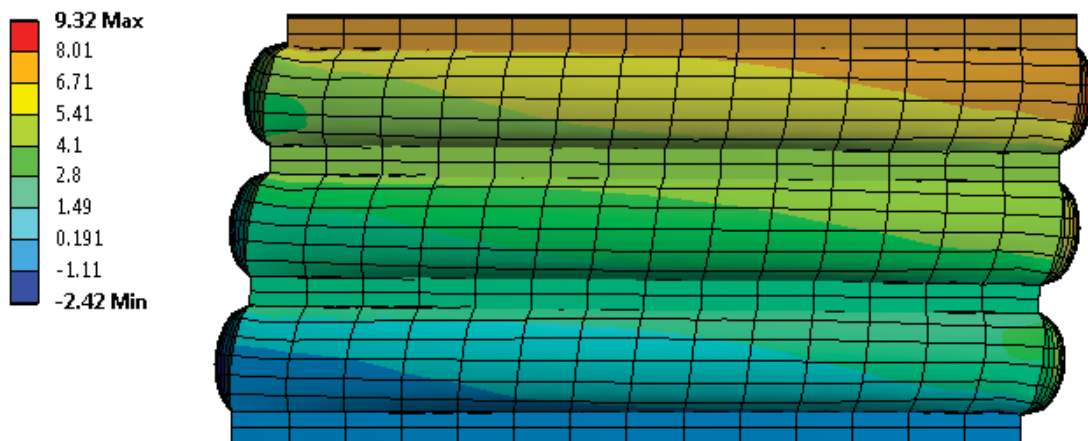


Figure 5.24 Deformed shape at 17% lateral strain (21<sup>st</sup> Step) (Under 4.5 MPa compression)

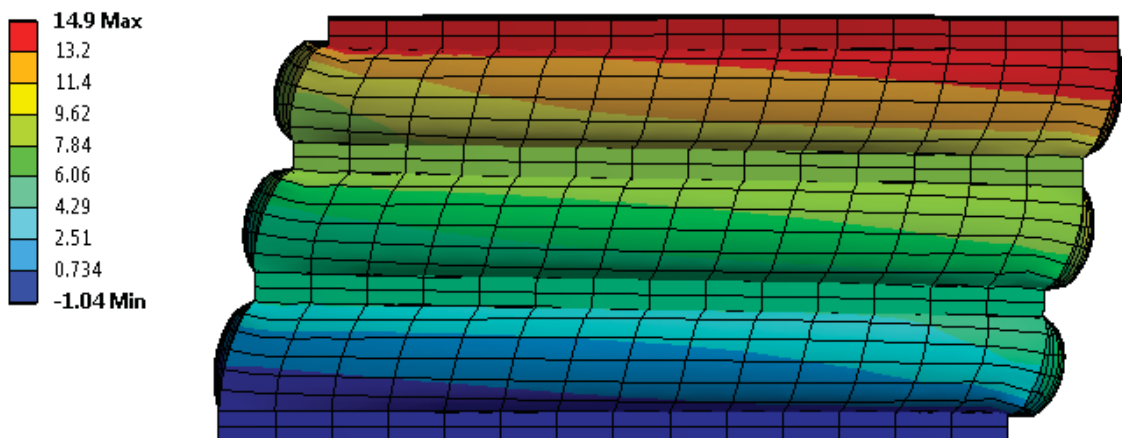


Figure 5.25 Deformed shape at 33% lateral strain (28<sup>st</sup> Step) (Under 4.5 MPa compression)

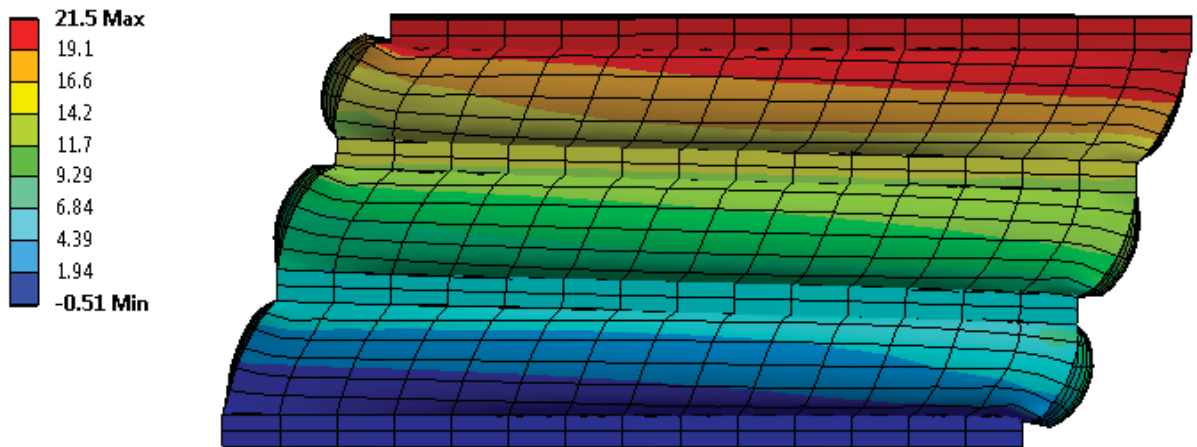


Figure 5.26 Deformed shape at 50% lateral strain (35<sup>th</sup> Step) (Under 4.5 MPa compression)

Table 5.3 Reaction forces at specified lateral strain level (4.5 MPa compression load)

Lateral Displacement (mm)	Reaction Force (kN)
7 (17% Strain)	1.16
14 (33% Strain)	2.26
21 (50% Strain)	3.35

### 5.5.1.2.3 Under 6 MPa Compression

Deformed shape of the finite element model after the specified step.

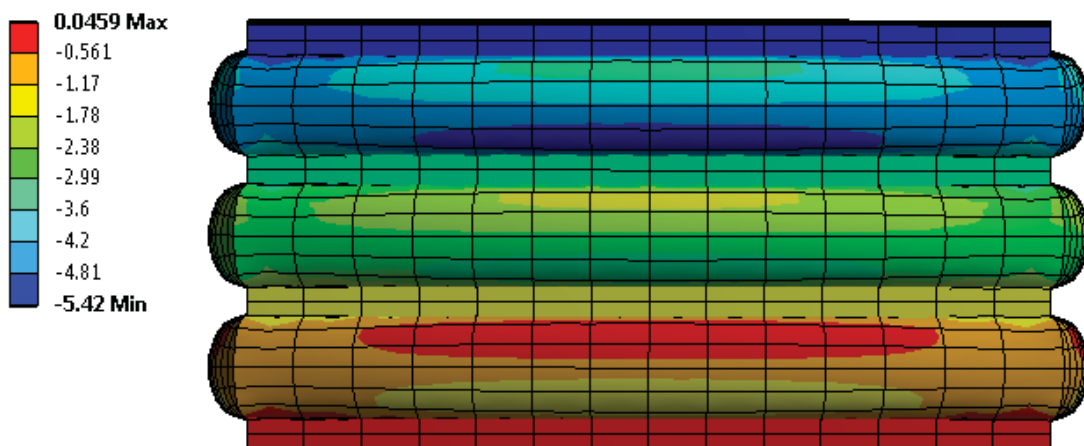


Figure 5.27 Axial deformation under 6 MPa compression load (14<sup>th</sup> Step)

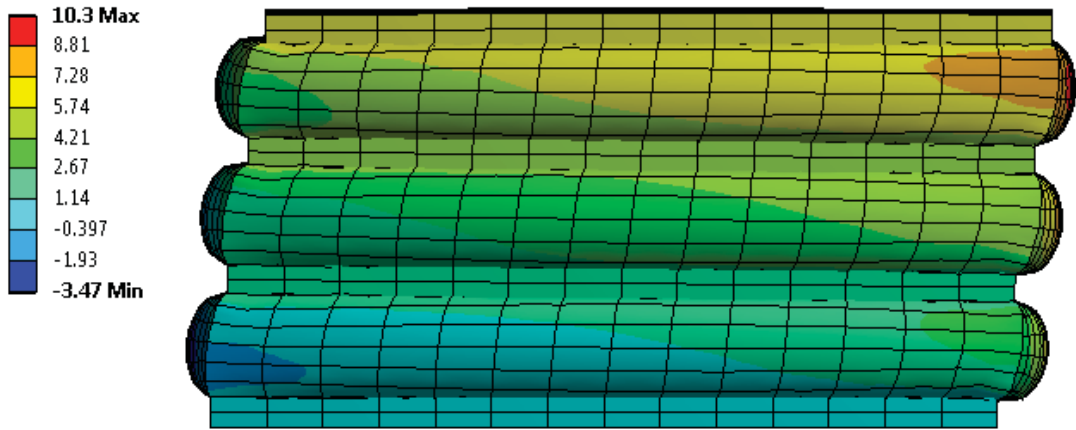


Figure 5.28 Deformed shape at 17% lateral strain (21<sup>st</sup> Step) (Under 6 MPa compression)

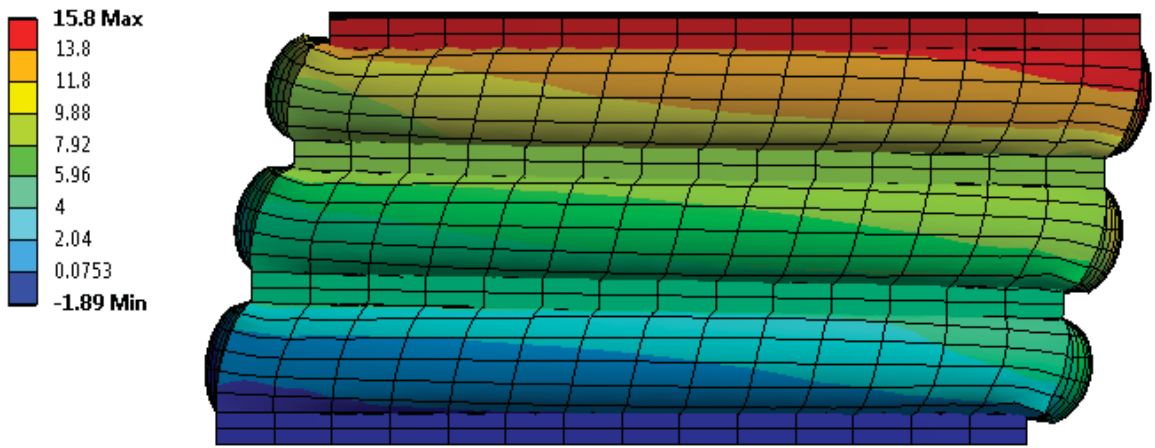


Figure 5.29 Deformed shape at 33% lateral strain (28<sup>th</sup> Step) (Under 6 MPa compression)

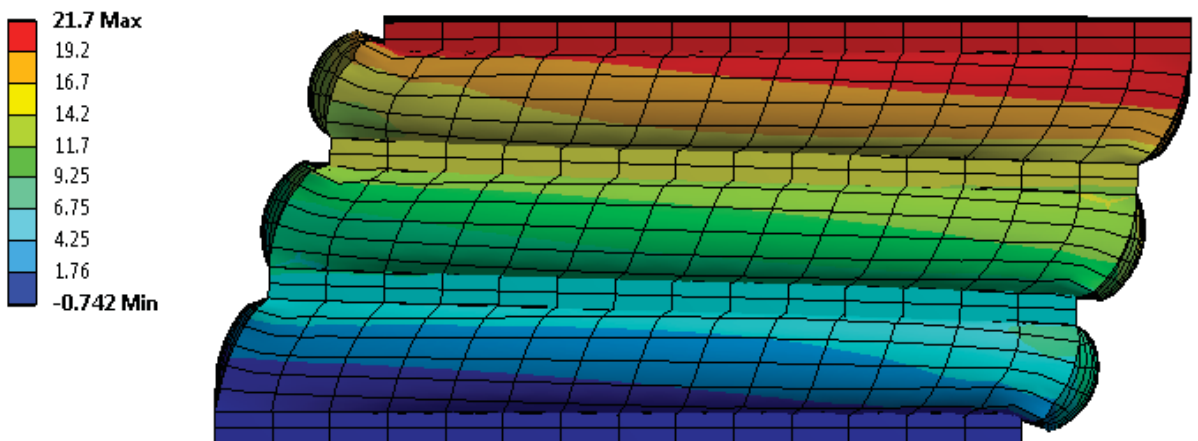


Figure 5.30 Deformed shape at 50% lateral strain (35<sup>th</sup> Step) (Under 6 MPa compression)

Table 5.4 Reaction forces at specified lateral strain level (6 MPa compression load)

Lateral Displacement (mm)	Reaction Force (kN)
7 (17% Strain)	0.92
14 (33% Strain)	1.76
21 (50% Strain)	2.59



RESULTS AND DISCUSSION

During the experimental studies executed after the determination of shear modulus, 10000 loading and release cycles were carried out for each different compression load levels. The force-displacement graphs given in the last pages of the related chapter demonstrate the required total load for horizontal movement on the specified cycle. Since these loads and the shear modulus are directly related, decrease on the required loads through the cycles indicate decreasing at shear modulus as well.

At the end of the chapter 4, the results data were demonstrated separately for specified cycles and each compression loads. Those graphs are combined below:

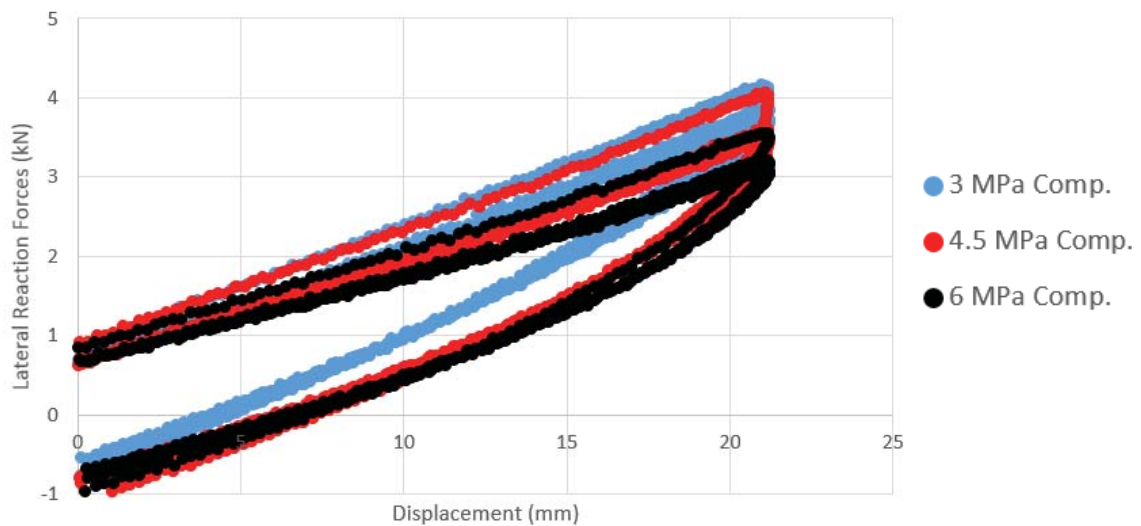


Figure 6.1 Change at lateral behavior through cycles (3 MPa compression)

It should be noted that as the graphs become closer to the horizontal axis, the bearing lose its lateral characteristics.



Three graphs given below shows the change at lateral behavior of a bearing through cycles, for each compression load levels separately.

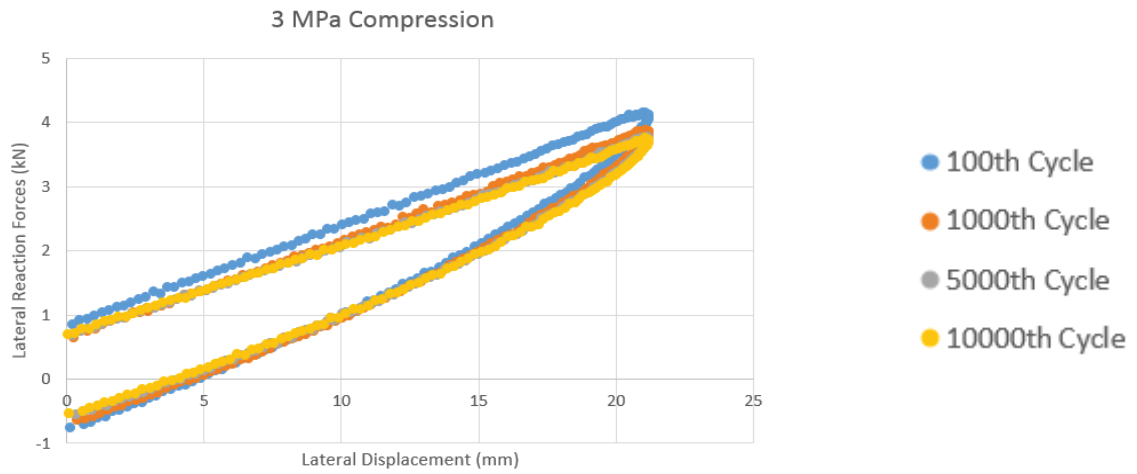


Figure 6.2 Change at lateral behavior through cycles (3 MPa compression)

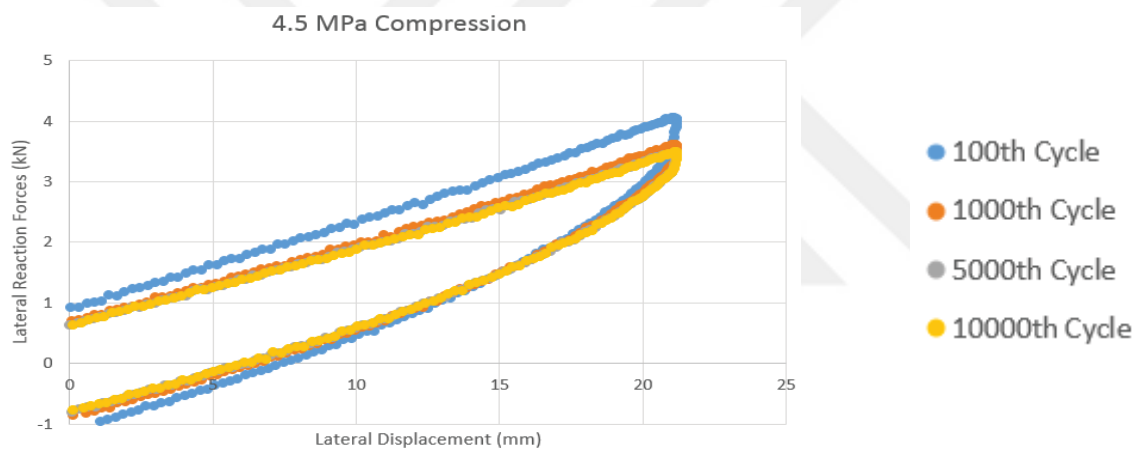


Figure 6.3 Change at lateral behavior through cycles (4.5 MPa compression)

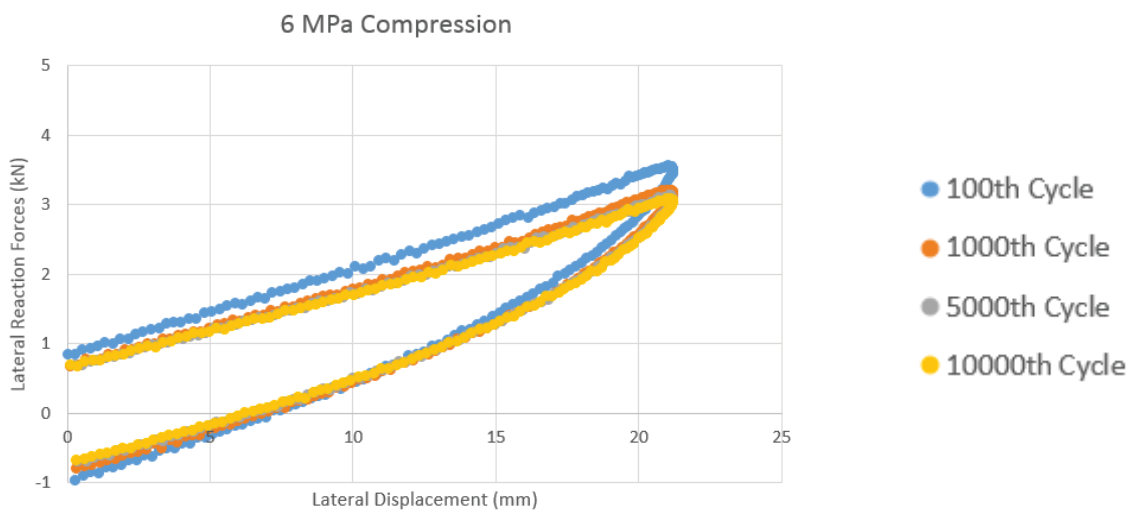


Figure 6.4 Change at lateral behavior through cycles (6 MPa compression)

Damping ratio of the bearings samples can be found out by using the hysteresis loops obtained during the cyclic loading. Formula for the determination of damping ratio is as follows:

$$\xi_{hyst} = \frac{A_{loop}}{2\pi F_{max} D_{max}} \quad (6.1)$$

Where  $\xi_{hyst}$  is damping ratio,  $A_{loop}$  is the area of the hysteresis loop,  $F_{max}$  and  $D_{max}$  are respectively, maximum force and displacements, obtained during the cyclic loading. Damping ratios of the bearing samples are demonstrated below:

Table 6.1 Damping ratios of bearing samples under specified conditions (%)

Cycle	Compression (Mpa)		
	3 MPa	4.5 MPa	6 Mpa
100	20.1	26	26.1
1000	17.6	22.1	24
5000	17	21	23
10000	16.9	21	22.9

Graphical demonstration of the table given above is as follows:

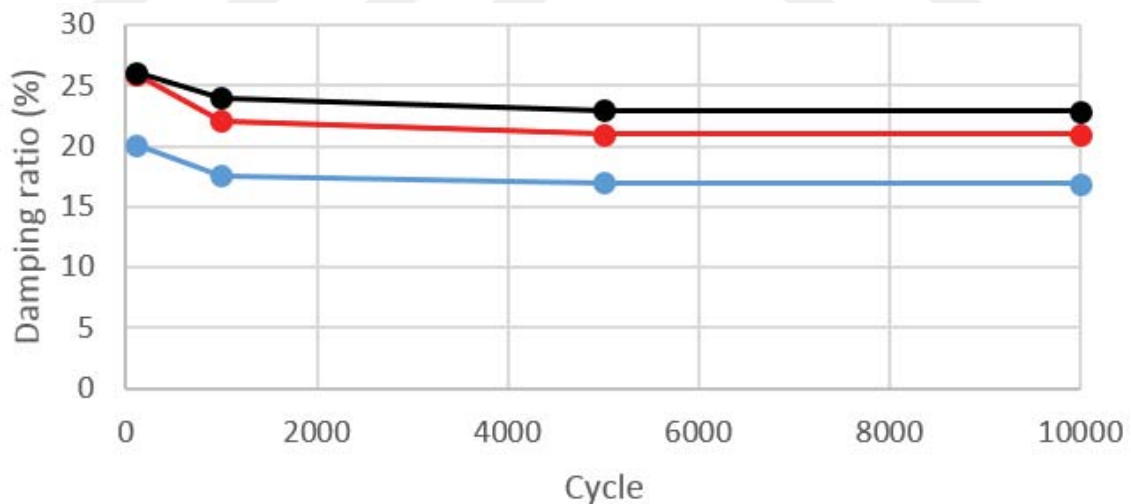


Figure 6.5 Graphical illustration of damping ratios through cycles under various compression loads

Damping ratios increased as more compression load applied. However, more cyclic loading has negative effect on damping ratio, but after a certain cycle number, bearing samples can keep their damping ratio characteristics. Similar behavior goes for the lateral stiffness as well, which is explained in following pages.

The graph given below should be examined to see the change at maximum reaction forces through cycles.

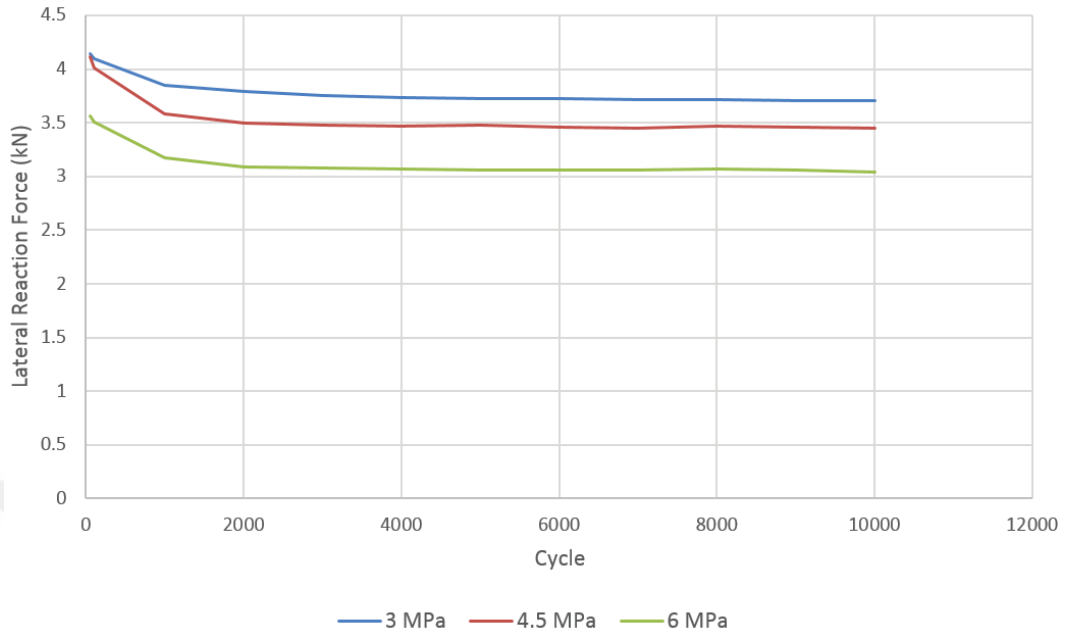


Figure 6.6 Change of maximum lateral reaction forces through cycles under 50% lateral strain (Experimental study)

This graph demonstrates the maximum loads that occurred during the lateral movement on every cycle. As can be observed, the behaviors of the bearing samples are quite similar to each other. Each of the samples' lateral stiffness are in almost linear noticeable decrease until around the 1000<sup>th</sup> cycle. After this cycle, the decrease stops and bearings have kept their lateral stiffness until the end of the experiment.

However, besides the similarity of the behaviors, the maximum loads differed related to the compression loads on bearings. The samples under 3 MPa compression load have the highest lateral stiffness, while the samples under 6 MPa compression load have the lowest.

Table given below shows the reaction forces occurred during the experimental study:

Table 6.2 Lateral reaction forces (kN) for each sample (Experimental study)

		Compression (MPa)								
		3			4.5			6		
Cycles	Lateral Deformation (mm)	7	14	21	7	14	21	7	14	21
	Strain	17%	33%	50%	17%	33%	50%	17%	33%	50%
	1	2.24	3.56	4.50	2.14	3.49	4.35	1.98	3.19	4.01
	50	2.07	3.04	4.14	2.00	3.01	4.11	1.74	2.62	3.57
	100	2.04	2.97	4.10	1.91	2.90	4.01	1.70	2.54	3.50
	1000	1.68	2.75	3.85	1.59	2.54	3.58	1.45	2.26	3.18
	2000	1.67	2.70	3.79	1.54	2.45	3.50	1.42	2.21	3.09
	3000	1.67	2.69	3.75	1.54	2.44	3.48	1.40	2.20	3.07
	4000	1.67	2.68	3.73	1.52	2.42	3.47	1.40	2.19	3.07
	5000	1.67	2.67	3.73	1.52	2.42	3.47	1.40	2.18	3.07
	6000	1.67	2.66	3.72	1.52	2.42	3.46	1.40	2.18	3.06
	7000	1.67	2.65	3.71	1.52	2.42	3.46	1.40	2.18	3.06
	8000	1.66	2.64	3.71	1.51	2.42	3.45	1.40	2.18	3.06
	9000	1.64	2.64	3.70	1.50	2.41	3.45	1.38	2.18	3.06
	10000	1.64	2.64	3.70	1.50	2.40	3.45	1.37	2.17	3.04

The graphical illustration of the table given above is as follows:

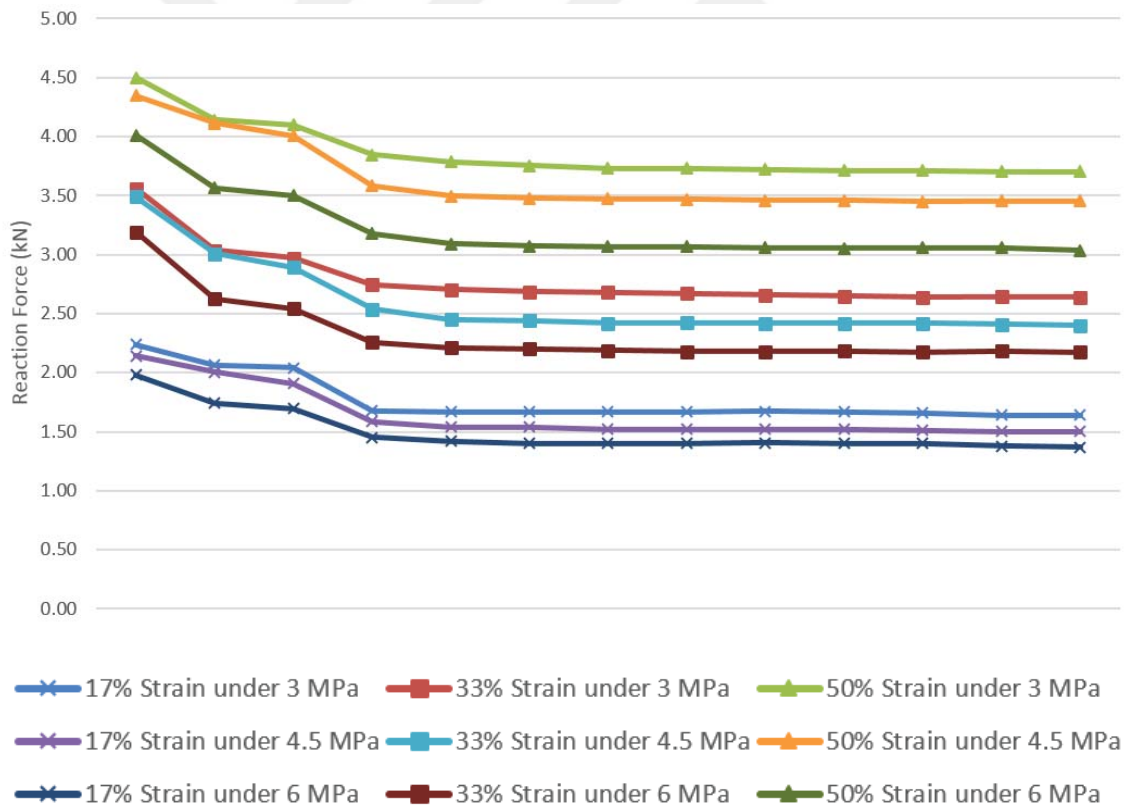


Figure 6.7 Lateral reaction forces (kN) through cycles for each sample (Experimental study)

According to the graph given above, the difference at lateral behavior between the bearing samples with different compression load has increased with the increasing strain levels.

After the experimental studies, finite element simulations based on the same conditions with experimental studies were carried out. Lacking the necessary data for rubber was tried to be overcome by modifying the uniaxial, biaxial and shear data of another rubber material using the shear data of the elastomeric bearing obtained from the related chapter. After the finite element model is prepared, the bearing model is forced to make lateral strain without compression load to see the pure lateral behavior. The experimental and simulation results are compared in the table given below:

Table 6.3 Lateral reaction forces without compression load

Lateral Displacement (mm)	Reaction Force (kN)		Relative Error (%)
	Experimental Results	Simulation Results	
7 (17% Strain)	1.81	1.49	17.68
14 (33% Strain)	3.12	3.11	0.32
21 (50% Strain)	4.32	4.75	9.95

Relative error values indicate the different behavior on the same strain levels between the modified stress-strain graph and the bearing. It can be inferred that 33% strain level (14 mm lateral displacement) is the intersection point of the modified stress-strain graph and bearing. Besides, the modified data has softer behavior at the beginning, but stiffer after the intersection point.

Later, the model is analyzed under compression loads. The comparison between the experimental and simulation results for each compression load level are given below:

Table 6.4 Axial displacements under specified compression load

Compression (MPa)	Axial Displacement (mm)		Relative Error (%)
	Experimental Result	Simulation Result	
3	4.33	3.20	26.10
4.5	6.20	4.37	29.52
6	7.70	5.42	29.61

Finally, the experiments executed in chapter 4.2 is tried to be simulated. The results and comparisons for each compression load level are demonstrated below:

Table 6.5 Comparisons of the results of experimental study and finite element model (3 MPa Compression)

		Compression (MPa)								
		3								
		Experimental Results			Simulation Results			Relative Error (%)		
Lateral Deformation (mm)		7	14	21	7	14	21	7	14	21
Strain		17%	33%	50%	17%	33%	50%	17%	33%	50%
Cycles	1	2.24	3.56	4.50	1.35	2.66	3.98	39.73	25.28	11.56
	50	2.07	3.04	4.14				34.66	12.40	3.91
	100	2.04	2.97	4.10				33.88	10.52	2.88
	1000	1.68	2.75	3.85				19.45	3.24	3.49
	2000	1.67	2.70	3.79				18.97	1.65	5.04
	3000	1.67	2.69	3.75				19.14	0.99	6.05
	4000	1.67	2.68	3.73				19.21	0.76	6.59
	5000	1.67	2.67	3.73				19.16	0.37	6.70
	6000	1.67	2.66	3.72				19.33	0.00	6.99
	7000	1.67	2.65	3.71				19.16	0.38	7.24
	8000	1.66	2.64	3.71				18.67	0.81	7.14
	9000	1.64	2.64	3.70				17.68	0.66	7.45
10000	1.64	2.64	3.70	17.68	0.76	7.51				

Table 6.6 Comparisons of the results of experimental study and finite element model (4.5 MPa Compression)

		Compression (MPa)								
		4.5								
		Experimental Results			Simulation Results			Relative Error (%)		
Lateral Deformation (mm)		7	14	21	7	14	21	7	14	21
Strain		17%	33%	50%	17%	33%	50%	17%	33%	50%
Cycles	1	2.14	3.49	4.35	1.16	2.26	3.35	45.79	35.24	22.99
	50	2.00	3.01	4.11				42.12	24.90	18.55
	100	1.91	2.90	4.01				39.12	21.95	16.44
	1000	1.59	2.54	3.58				26.83	10.99	6.46
	2000	1.54	2.45	3.50				24.60	7.76	4.18
	3000	1.54	2.44	3.48				24.53	7.38	3.74
	4000	1.52	2.42	3.47				23.73	6.61	3.50
	5000	1.52	2.42	3.47				23.84	6.65	3.46
	6000	1.52	2.42	3.46				23.68	6.61	3.21
	7000	1.52	2.42	3.46				23.68	6.61	3.18
	8000	1.51	2.42	3.45				23.28	6.61	2.90
	9000	1.50	2.41	3.45				22.67	6.22	3.03
10000	1.50	2.40	3.45	22.67	5.83	3.02				

Table 6.7 Comparisons of the results of experimental study and finite element model (6 MPa Compression)

		Compression (MPa)								
		6								
		Experimental Results			Simulation Results			Relative Error (%)		
Lateral Deformation (mm)		7	14	21	7	14	21	7	14	21
Strain		17%	33%	50%	17%	33%	50%	17%	33%	50%
Cycles	1	1.98	3.19	4.01	0.92	1.76	2.59	53.54	44.83	35.41
	50	1.74	2.62	3.57				47.15	32.94	27.39
	100	1.70	2.54	3.50				45.85	30.74	26.06
	1000	1.45	2.26	3.18				36.67	22.09	18.47
	2000	1.42	2.21	3.09				35.30	20.36	16.18
	3000	1.40	2.20	3.07				34.44	20.01	15.77
	4000	1.40	2.19	3.07				34.29	19.63	15.57
	5000	1.40	2.18	3.07				34.23	19.27	15.64
	6000	1.40	2.18	3.06				34.50	19.27	15.36
	7000	1.40	2.18	3.06				34.36	19.32	15.25
	8000	1.40	2.18	3.06				34.37	19.17	15.36
	9000	1.38	2.18	3.06				33.33	19.38	15.28
10000	1.37	2.17	3.04	32.69	19.04	14.70				

Although being lack of some test data for rubber material, accurate results were achieved –especially for lateral behavior- on certain strain levels. However, the material constants were not sufficient to simulate compression behavior. This situation caused higher relative errors as the compression loads increased. Executing uniaxial, biaxial and volumetric tests for the rubber material provides the compression behavior to be simulated much more accurately.

Conclusions of the studies executed in this thesis are summarized below:

- Same types of elastomeric bearings have nearly the same lateral behavior no matter what the compression load applied to them. However, the value of lateral stiffness decreases as the compression load increases. Lateral stiffness has linear noticeable decrease until the certain level of cycle but bearings can keep their “ultimate lateral stiffness” afterwards.
- This ultimate lateral stiffness may be used for designing highly dynamic structures such as bridges and viaducts since the bearings are under continuous movement under these structures compared to other types of buildings.
- During the design process of a structure with base isolation, the compression loads on each bearing and their working efficiency as a group should be taken into account since their lateral stiffness may differ from each other greatly due to the various compression loads.
- Difference at lateral stiffness of elastomeric bearings under various compression loads increases as the lateral strain level increases.
- Using the modified stress-strain graphs for uniaxial, biaxial and shear behaviors works successfully for simulating the lateral behavior until a certain level of compression load and lateral strain. The finite element analysis without a compression load shows that the behaviors of the modified data and actual bearing have perfectly matched at 33% strain level (14 mm lateral displacement). However, the bearing has softer lateral behavior at the beginning, but stiffer after the intersection point (33% strain level).
- The material constants obtained from the modified stress-strain graphs were not sufficient to simulate compression behavior as accurate as the lateral behavior. This situation caused higher relative errors as the compression loads increased.

Executing uniaxial, biaxial and volumetric tests for the rubber material provides the results for compression behavior to be more accurate.

- As a future work, executing the essential tests for elastomer material provides to simulate the bearings in various conditions with quite reasonable relative errors.





## REFERENCES

- 
- [1] Disaster & Emergency Management Authority of Republic of Turkey, Presidential of Earthquake Department, Earthquake Catalog, <https://deprem.afad.gov.tr/depremkatalogu?lang=en>, April 13, 2019.
- [2] Yura, J., Kumar, A., Yakut, A., Topkaya, C., Becker, E, Collingwood, J., (2001). NCHRP report 449: Elastomeric Bridge Bearings: Recommended Test Methods, Transportation Research Board, Washington, DC.
- [3] Tafheem, Z., Arafat, T., Chowdhury, A., Iqbal, A., (2015). “Seismic Isolation Systems in Structures-the State of Art Review”, Proceedings of 11<sup>th</sup> Global Engineering, Science and Technology Conference, 18-19 December, 2015, Dhaka, Bangladesh.
- [4] Taylor, A. W., Igusa, T. (Eds.) (2004). Primer on seismic isolation, ASCE publications.
- [5] Gandelli, E., (2017). Advanced tools for the design of sliding isolation systems for seismic-retrofitting of hospitals, Doctoral dissertation, Politecnico di Milano, Built Environment and Construction Engineering.
- [6] Maalek, S., Akbari, R., Ziaei-Rad, S. (2007). “Estimation of elastomeric bridge bearing shear modulus using operational modal analysis”, 2<sup>nd</sup> international operational modal analysis conference, IOMAC. 2007, Denmark.
- [7] Elghazouli, A. (2016). Seismic design of buildings to Eurocode 8, Second edition, CRC Press.
- [8] Kamrava, A., (2015). “Seismic Isolators and their types”, Current world environment, 10, 27-32.
- [9] Skinner, R. I., Robinson, W. H., McVerry, G. H. (1993). An introduction to seismic isolation, John Wiley & Sons.
- [10] Michael, R. J. (2013). Design and Development of a Seismic Isolation System for Commercial Storage Racks, Doctoral dissertation, Case Western Reserve University, Department of Mechanical and Aerospace Engineering.
- [11] Pall Dynamics Limited, Pall Friction Dampers, [http://www.palldynamics.com/SeismicDampers\\_ViscousDampers\\_EnergyDissipatingDevices.htm](http://www.palldynamics.com/SeismicDampers_ViscousDampers_EnergyDissipatingDevices.htm), April 13, 2019.
- [12] Zaogiang Dacheng Rubber Co., Ltd., Laminated Elastomeric Bearing Pad: High Vertical Load, <http://www.bridgebearing.org/bridgebearing/laminated-elastomeric-bearing-pad.html>, April 03, 2018.

- [13] ASTM D4014-03, (2018). Standard Specifications for Plain and Steel-Laminated Elastomeric Bearings for Bridges, ASTM International, West Conshohocken, PA, 2018, [www.astm.org](http://www.astm.org)
- [14] Smooth-On, Durometer Shore Hardness Scale, <https://www.smooth-on.com/page/durometer-shore-hardness-scale/>, April 13, 2019.
- [15] ASTM D2240-15e1, Standard Test Method for Rubber Property—Durometer Hardness, ASTM International, West Conshohocken, PA, 2015, [www.astm.org](http://www.astm.org)
- [16] PTC Instruments, What is a Durometer, [http://ptc1.com/what\\_is\\_durometer.htm](http://ptc1.com/what_is_durometer.htm), April 13, 2019.
- [17] ASTM D1415-18, Standard Test Method for Rubber Property—International Hardness, ASTM International, West Conshohocken, PA, 2018, [www.astm.org](http://www.astm.org)
- [18] Stanton, J. F., Roeder, C. W. (1982). Elastomeric bearings design, construction, and materials, NCHRP report, (248).
- [19] Roeder, C. W., Stanton, J. F., Taylor, A. W., Performance of Elastomeric Bearings, (1987). NCHRP Report 298, TRB, National Research Council, Washington, D.C., October 1987.
- [20] Lee, D. J. (1994): Bridge bearings and expansion joints, CRC Press.
- [21] Zakariaei, P. (2005). Monotonic and hysteretic behavior of elastomeric bridge bearings, MSc Thesis, Tehran University.
- [21] AASHTO M 251-06, (2006). Standard Specification for Plain and Laminated Elastomeric Bridge Bearings, AASHTO, USA.

## CURRICULUM VITAE

---

### PERSONAL INFORMATION

**Name Surname** : Kadir EKŞİ  
**Date of birth and place** : 08.03.1994, Sakarya  
**Foreign Languages** : English  
**E-mail** : kadir.eksi12@gmail.com

### EDUCATION

<b>Degree</b>	<b>Department</b>	<b>University</b>	<b>Date of Graduation</b>
Undergraduate	Civil Engineering	Yıldız Technical University	2016
High School	Natural Sciences	Figen Sakallıoğlu Anatolian High School	2012

### WORK EXPERIENCE

<b>Year</b>	<b>Corporation/Institute</b>	<b>Enrollment</b>
2016-	Metal Yapı A.Ş.	Façade Engineer